Cross-dataset reproducibility of population receptive field (pRF) estimates and cortical magnification asymmetries

Authors and affiliations: Marc M. Himmelberg[1†], Jan W. Kurzawski[1†], Noah C. Benson[2], Denis G. Pelli[1,3], Marisa Carrasco[1,3,] & Jonathan Winawer[1,3]

[1] Department of Psychology, New York University, New York, NY, USA, 10003
[2] eScience Institute, University of Washington, Seattle, WA, USA, 98122
[3] Center for Neural Sciences, New York University, New York, NY, USA, 10003
[†] Both authors contributed equally

Corresponding Author: Marc M. Himmelberg, Department of Psychology, 6 Washington Place, New York University, NY, 10003 (marc.himmelberg@nyu.edu)

Conflict of interest: The authors declare no competing financial interests.

Keywords: retinotopy, pRF mapping, cortical magnification, performance fields, reproducibility

Funding: This research was funded by the US National Eye Institute R01-EY027401 to MC and JW and R01EY027964 to DGP.

Abstract

Population receptive field (pRF) models fit to fMRI data are used to non-invasively measure retinotopic maps in human visual cortex, and these maps are a fundamental component of visual neuroscience experiments. We examined the reproducibility of retinotopic maps across two datasets: a newly acquired retinotopy dataset from New York University (NYU) (n=44) and a public dataset from the Human Connectome Project (HCP) (n=181). Our goal was to assess the degree to which pRF properties are similar across datasets, despite substantial differences in their experimental protocols. The two datasets differ in stimulus design, participant pool, fMRI protocol, MRI field strength, and preprocessing pipelines. We assessed the cross-dataset reproducibility of the two datasets in terms of the similarity of vertex-wise pRF estimates and in terms of large-scale cortical magnification properties. Within V1, V2, V3, and hV4, the group-median NYU and HCP vertex-wise polar angle estimates were nearly identical. Both eccentricity and pRF size estimates were also strongly correlated between the two datasets, but with a slope different from 1; the eccentricity and pRF size estimates were systematically greater in the NYU data. Next, to compare large-scale map properties, we quantified two polar angle asymmetries in V1 cortical magnification previously identified in the HCP data. The prior work reported more cortical surface area representing the horizontal than vertical visual field meridian, and the lower than upper vertical visual field meridian. We confirm both of these results in the NYU dataset. Together, our findings show that the retinotopic properties of V1-hV4 can be reliably measured between two datasets, despite numerous differences in their experimental design. fMRI-derived retinotopic maps are reproducible because they rely on an explicit computational model that is grounded in physiological evidence of how visual receptive fields are organized, allowing one to quantitatively characterize the BOLD signal in terms of stimulus properties (i.e., location and size). The new NYU Retinotopy Dataset will serve as a useful benchmark for testing hypotheses about the organization of visual areas and for comparison to the HCP Retinotopy Dataset.

Introduction

The human visual system preserves image structure in cortical maps of the visual field. These retinotopic maps are the basis by which measurements across labs, populations, and tasks are compared. Functional magnetic resonance imaging (fMRI) has made it possible to non-invasively measure these maps from visually evoked activity in human cortex (DeYoe et al., 1994; Engel et al., 1994; Sereno et al., 1995). Advances in these methods have led to sophisticated models such as population receptive field (pRF) modeling (Dumoulin & Wandell, 2008), which has become a core component of experiments investigating human visual cortex (reviewed by Wandell & Winawer (2015).

Recently, the Human Connectome Project (HCP) 7 Tesla Retinotopy Dataset has been made available for public use (Benson et al., 2018). This dataset contains high-quality retinotopy data from 181 participants, collected with 7T magnetic resonance imaging (MRI), with 30 minutes of data per participant. The high quality and large size of the dataset make it an attractive resource for researchers to address a wide variety of questions. It has been used to investigate retinotopic organization in visual cortex, including the organization of core pRF parameters (Benson et al., 2018), the organization of white matter connections between thalamus and foveal and peripheral representations of extrastriate cortex (Kurzawski et al., 2020), the identification new retinotopic maps in the cerebellum (van Es et al., 2019) and hippocampus (Silson et al., 2021), visual organization in the default network (Szinte & Knapen, 2020), and polar angle meridian asymmetries in cortical magnification in primary visual cortex (V1) (Benson et al., 2020). One benefit of the HCP dataset is that its large size permits researchers to conduct checks of internal reliability. For example, if a finding is observed in one half of the participant sample, is it also observed in the other half? However, these internal checks rely on data that have been collected using the same MRI scanner, preprocessed via the same pipeline, and analyzed using the same pRF software. Therefore, systematic biases affecting a full dataset could make the data internally reliable, but not generalizable.

Visual neuroscientists assume that retinotopic organization is broadly consistent across the healthy human population. Previous studies have validated the reliability of retinotopic properties within their own datasets (Benson et al., 2018; Binda et al., 2013; Senden et al., 2014; van Dijk et al., 2016; Zeidman et al., 2018; Zuiderbaan et al., 2012). However, it is important to validate scientific findings relating to retinotopic organization by testing whether they can be reproduced in *independent datasets*. One robust assessment of the validity of such findings is via their reproduction in a retinotopy dataset that uses a different MRI scanner, fMRI protocol, stimulus design, and preprocessing pipeline. Such differences are typical in neuroimaging studies across labs. To our knowledge, an explicit test of the reproducibility of retinotopic maps between datasets differing in many aspects has not been conducted. To measure the reliability of retinotopic maps across independent datasets, we have acquired, and made publicly available, a large new set of retinotopic data (the New York University (NYU) Retinotopy Dataset) that differs from the HCP data in many ways.

Here, we test the cross-dataset reproducibility of retinotopic maps at two scales of analysis; a fine scale (vertex-wise pRF estimates) and a large-scale (the surface area of extended cortical regions). Retinotopic maps are differentiated based on polar angle and eccentricity representations of the visual field (Dumoulin & Wandell, 2008; Wandell et al., 2007). Thus, we first consider the cross-dataset reproducibility of vertex-wise pRF estimates (polar angle, eccentricity, and pRF size) between the NYU and HCP data. We do so in four visual areas: V1,

V2, V3, and hV4. To make vertex-wise comparisons between the two datasets, all individual cortical surfaces are aligned to a template surface and the native geometry of the individuals is discarded. We then compare pRF parameters at each vertex between the two datasets. Second, we examine large-scale properties of the maps in terms of surface area. Findings from the HCP dataset show large-scale polar angle asymmetries in V1 cortical magnification: substantially more cortical surface area is dedicated to processing the horizontal than the vertical visual field meridian (the horizontal-vertical anisotropy; HVA), and there is more cortical surface area dedicated to the lower than the upper vertical visual field meridian (the vertical meridian asymmetry; VMA) (Benson et al., 2020). Here, we assess the HVA and VMA in V1 cortical magnification in our new (NYU) dataset. The cortical magnification measures reflect the relation between retinotopic coordinates and cortical geometry (local surface area) and therefore, unlike the vertex-wise comparisons, require analysis on each participant's native cortical surface.

Methods

Participants

44 participants (25 females, 19 males, mean age=28.8 years) were recruited from New York University (NYU). All participants had normal or corrected-to-normal vision and completed a 1 – 1.5-hour scanning session. All participants provided written informed consent and approved the public release of anonymized data. The experiment was conducted in accordance with the Declaration of Helsinki and was approved by the NYU ethics committee on activities involving human participants.

fMRI stimulus display

Participants viewed the pRF stimulus in the MRI scanner using a ProPixx DLP LED projector (VPixx Technologies Inc., Saint-Bruno-de-Montarville, QC, Canada). The stimulus image was projected onto an acrylic back-projection screen (60 cm x 36.2 cm) in the scanner bore. The projected image had a resolution of 1920 × 1080 and a refresh rate of 60 Hz. The display was calibrated using a linearized lookup table. Participants viewed the screen at a distance of ~83.5 cm (from eyes to the screen) using an angled mirror that was mounted on the head coil.

PRF Stimulus

The PRF stimulus was generated in MATLAB 2017a and was presented using the Psychophysics Toolbox v3 (Kleiner et al., 2007) and custom *vistadisp* software (https://github.com/WinawerLab/vistadisp) on an iMac computer. Stimulus image patterns were shown within a bar aperture that swept across the screen throughout each scan. There were 100 stimulus image patterns. These stimulus images were identical to those used in the HCP 7T Retinotopy project, except for the rescaling to the size of our display. Each image pattern was composed of colorful objects, faces, and scenes at multiple scales (Kriegeskorte, 2008) that were superimposed on an achromatic pink-noise (1/f) background (see **Figure 1A** for example of the pRF stimulus). The stimulus image pattern was windowed within a circular aperture (12.4° radius) and was revealed through the bar aperture that swept across the screen in 24 equal steps, once per second, synchronized to the MR image acquisition (TR=1 second). The bar aperture was superimposed on a polar fixation grid placed upon a uniform gray background, with a red or green dot at the center (3 pixels, or 0.07°). The polar grid and small fixation point

were used to encourage good fixation behavior, as previously described (Schira et al., 2009). The bar aperture was 3.1° in width, which was 1/8th of the full stimulus extent (24.8° diameter). The bar aperture swept across the screen in 8 directions (see **Figure 1B** for sweep direction order and timings). Each sweep began at the edge of the circular aperture. Horizontal and vertical sweeps traversed the entire diameter of the aperture. Diagonal sweeps only traversed half of the aperture (the second half of the sweep was replaced with a blank gray screen, other than the fixation dot and grid). The blank periods help discriminate between nonvisual responses and responses from populations of neurons with exceptionally large receptive field sizes (Dumoulin & Wandell, 2008).

Each directional sweep lasted 24 seconds, with the full stimulus run lasting 192 seconds. The stimulus image updated 3 times per second without intermediate blanks, thus the three images were shown for 0.333 seconds at each aperture position. Participants completed a fixation task to ensure that they were maintaining central fixation and remained alert throughout the scan. Participants were required to respond, via button press, when the central fixation dot changed from green to red, or vice versa. The full stimulus sequence was completed once per scan, and 4 to 12 scans were collected per participant, with the identical aperture sequence in each of the repeated scans.

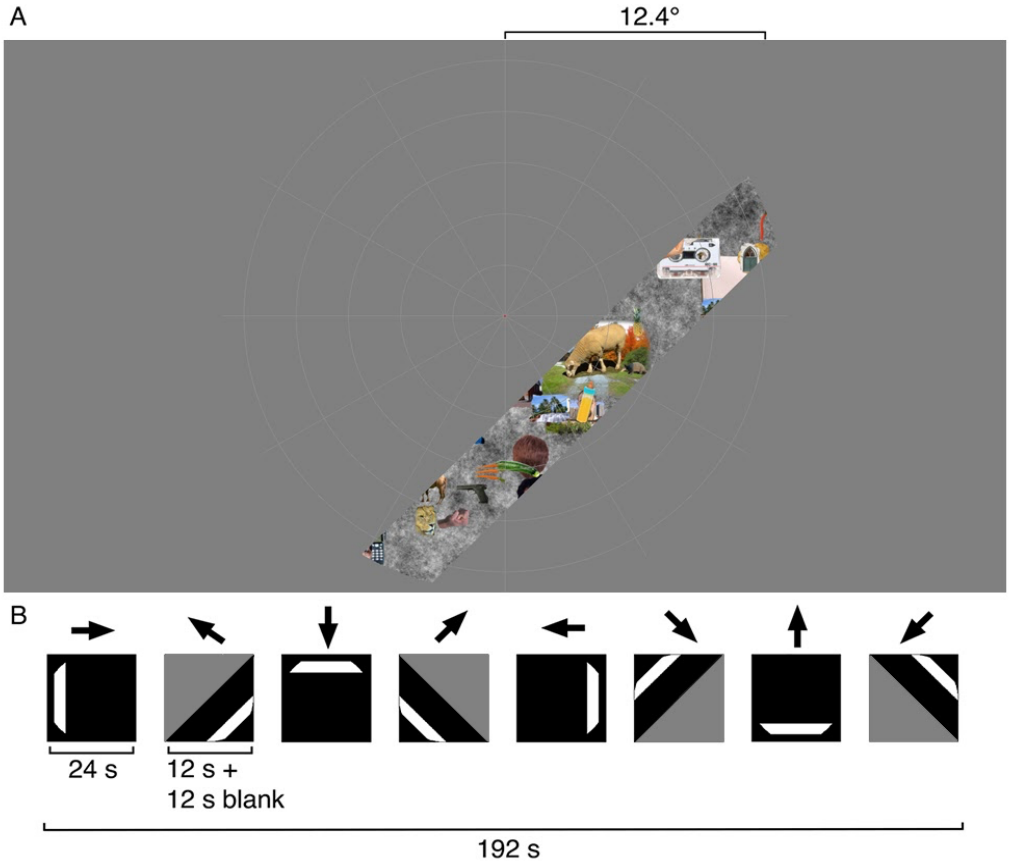

Figure 1. Example of the pRF stimulus and experimental design. (**A**) The pRF stimulus at a single time point. The bar aperture reveals the stimulus image pattern composed of colorful objects, faces, and scenes at different scales, randomly placed across an achromatic pink noise background. The fixation-point at the center of the fixation grid changes from green to red and red to green at random time points. (**B**) Experimental design for a single scan across 192 s – the pRF bar is swept across the screen in eight cardinal directions, with each directional sweep lasting 24 seconds. Gray triangles indicate blank periods. Black regions correspond to the visual field covered by the sweeping bar (excluding the stimulus aperture).

Structural and functional data acquisition

Structural and functional data were acquired on a 3T Siemens MAGNETOM Prisma MRI scanner (Siemens Medical Solutions, Erlangen, Germany) at the Center for Brain Imaging at NYU. Both the structural and functional images were acquired using a Siemens 64-channel head coil. Between 1 and 2 full brain T1-weighted (T1w) MPRAGE anatomical images were acquired for each participant (TR, 2400 ms; TE, 2.4 ms; voxel size, 0.8mm^3 isotropic; flip angle, 8°), auto-aligned to a template to ensure a similar slice prescription for all participants. For a subset of participants (n = 11) for whom there was sufficient time in the scanning session, a full brain T2-weighted (T2w) anatomical image was obtained to aid in automatic segmentation (TR, 3200 ms; TE, 564 ms; voxel size, voxel size, 0.9mm^3 isotropic; flip angle, 120°). Between 4 and 12 functional echo-planar images (EPIs) were acquired for each participant using a T2*-weighted multiband EPI sequence (TR, 1000 ms; TE, 37 ms; voxel size, 2mm^3; flip angle, 68°; multiband acceleration factor, 6; phase-encoding, posterior-anterior) (Feinberg et al., 2010; Xu et al., 2013). Additionally, two distortion maps were acquired to correct susceptibility distortions in the functional images: one spin-echo image with anterior-posterior (AP) and one with posterior-anterior (PA) phase encoding.

Preprocessing of structural and functional data using fMRIPrep

Anatomical and functional preprocessing was performed using *fMRIPrep* v.20.0.1 (Esteban et al., 2019; Gorgolewski et al., 2011). Each T1w anatomical image was corrected for intensity inhomogeneity and was skull-stripped. Automatic brain segmentation of cerebrospinal fluid, white-matter, and gray-matter was performed on the skull-stripped T1w image using *fast* (Zhang et al., 2001). If acquired, the T2w image was included as an additional input for brain segmentation. Cortical surfaces were then reconstructed using Freesurfer's *recon-all* (Dale et al., 1999) and an estimated brain mask was refined using a custom variation of the method.

For each participant's functional images, the following preprocessing was performed. First, a reference volume and its skull-stripped version were created using the custom methodology from *fMRIPrep*. A B0-nonuniformity map was estimated based on the two spin-echo images with opposing phase-encoding directions (i.e., the AP and PA distortion maps). Using the estimated distortion, a corrected functional reference image was calculated to ensure accurate co-registration with the anatomical reference. The functional reference was co-registered to the T1w anatomical reference. Co-registration was configured with six degrees of freedom. Head-motion parameters with respect to the functional reference (transformation matrices, and six corresponding rotation and translation parameters) were estimated before any spatiotemporal filtering. The functional images were then slice-time corrected.

Next, the time-series data from the functional images were resampled onto the FreeSurfer *fsnative* and *fsaverage* surfaces by applying a single, composite transform to correct for head-motion and susceptibility distortions. Thus, the resampling was performed in a one-shot interpolation by composing all the pertinent transformations (i.e., head-motion transform matrices, susceptibility distortion correction, and co-registrations to *fsnative* and *fsaverage* output spaces).

Population receptive field model

PRF analysis was conducted using *vistasoft* (https://vistalab.stanford.edu/software/, Vista Lab, Stanford University). Here, a pRF is modelled as a circular 2D-Gaussian, as described in

Dumoulin and Wandell (2008). The Gaussian is parameterized by values at each vertex for x, y, and σ. The x and y parameters specify the center position of the 2D-Gaussian in the visual field. The σ parameter, the standard deviation of the 2D-Gaussian, specifies the size (or spread) of the receptive field. The 2D-Gaussian is multiplied pointwise by the stimulus contrast aperture, and then convolved with a hemodynamic response function (HRF) to predict the BOLD percent signal change (or 'BOLD signal'). The HRF is parameterized by 5 values, describing a difference of two gamma functions, as used previously (Dumoulin & Wandell, 2008; Friston et al., 1998; Harvey & Dumoulin, 2011; Worsley et al., 2002). The HRF was assumed to be the same across vertices within a participant but differed among participants.

The *vistasoft* pRF model was implemented using the *prf-analyze-vista* docker container (https://github.com/vistalab/prfmodel; Lerma-Usabiaga et al., 2020). The software finds the optimal pRF parameters for each vertex, and the optimal HRF parameters averaged across vertices, by minimizing the residual sum of squares between the predicted time-series and the BOLD signal. This is completed using a multi-stage coarse-to-fine approach. The basic two-stage coarse-to-fine component is described in detail by Dumoulin and Wandell (2008), and the addition of the HRF fit is described in detail by Harvey and Dumoulin (2011). In brief, in the first stage, the data were temporally decimated by a factor of two to remove high frequency noise and the pRF parameters (x, y, and σ) were fit by a brute force grid search. The results of this fit were taken as the starting point of a second-stage search fit for these parameters using the full time-series. The pRF parameters were then held fixed and the HRF parameters were fit by a search, choosing the parameters that minimize the squared error between data and prediction averaged across vertices. Finally, the HRF parameters were held fixed and the pRF parameters were refit.

We implemented the pRF model on three formats of data. First, we solved the pRF model for each vertex on individual participant data to produce pRF maps on *fsnative* surfaces. Second, for each participant, we interpolated the results by nearest neighbor from the *fsnative* space to the *fsaverage* space. This interpolation puts the model solutions for all participants in the same brain space, enabling us to derive the vertex-wise median parameters across participants. Third, we solved pRF models for each vertex on the time-series averaged across all participants to compute group-average pRF maps on the *fsaverage* surface. The second and third methods differ in the order of operations: the second computes median parameters from all individual participants' time series, and the third computes a single set of parameters on the averaged time series. These three implementations are described in detail below.

Implementing the pRF model: Individual participants and the parameter-median data

First, we solved the pRF model for individual participants on their *fsnative* surface. For each participant, the time-series data across multiple scans with the same stimulus were averaged to create a participant-averaged time-series. The participant-averaged time-series was then transformed to BOLD percent signal change (i.e., percent change at each TR from the mean signal across all TRs). We fit the pRF model to this BOLD percent signal change. An example of the pRF model fit to an individual participant's BOLD signal from a V1 and a V2 vertex is shown in **Figure 2A** and **B**.

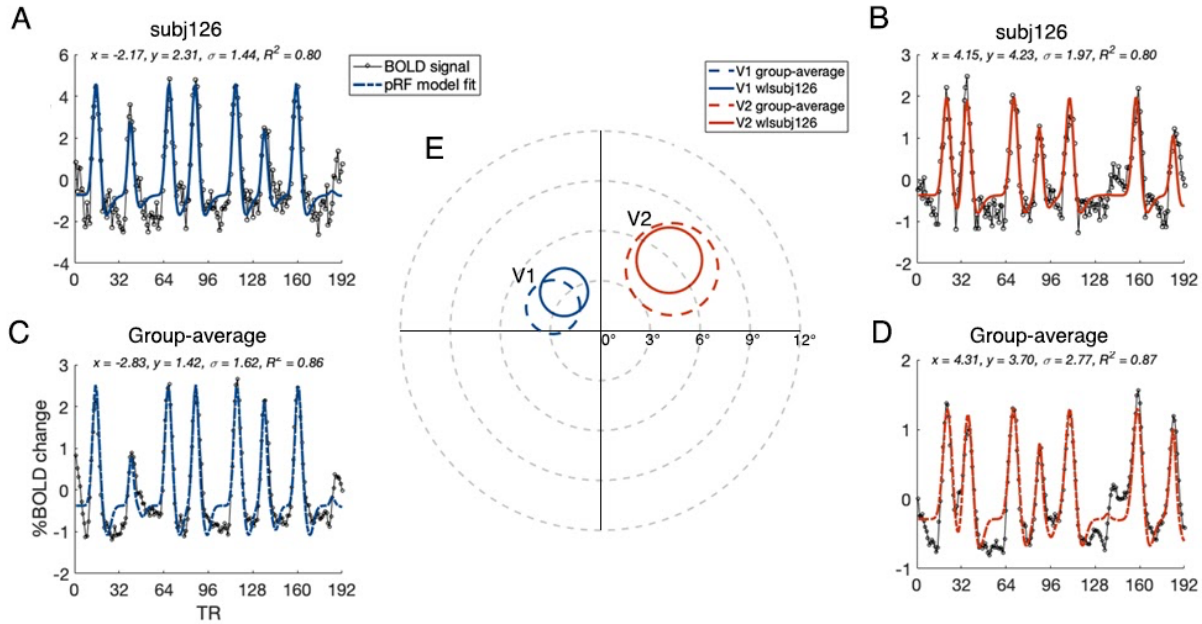

Figure 2. Examples of the pRF model fit to an individual participant's (wlsubj126) and the group-average BOLD percent signal change for two example fsaverage vertices in V1 and V2. (**A-B**) The BOLD signal and pRF model fit for a V1 and V2 vertex for an individual participant. (**C-D**) The BOLD signal and pRF model fit for a V1 and V2 vertex for the group-average time-series data. (**E**) Visual field representation with pRFs plotted for V1 and V2. The inset text lists the predicted *x* and *y* values, representing the pRF center coordinates (in degrees), and the σ value, representing the pRF size (in degrees), and the R^2 which is the variance explained of the pRF model fit to the BOLD signal.

Next, we computed parameter-median pRF maps. These maps were used to complete vertex-wise comparisons between the NYU and HCP data. We used the FreeSurfer function *mri_surf2surf* to interpolate the pRF parameters by nearest neighbor from each participant's *fsnative* surface onto an *fsaverage* surface. To generate the parameter-median polar angle and eccentricity maps, we calculated the median *x*, *y,* and *σ* values for each *fsaverage* vertex across all participants and converted these values to polar angle, eccentricity, and pRF size parameters.

Implementing the pRF model: The group-average time-series data

We implemented the pRF model on group-averaged time-series data for map visualization and for visual comparison with the HCP data, which also include group-average time series and pRF model solutions (Benson et al, 2018).

We generated the group-average time-series as the vertex-wise average of each participants' average time-series on the *fsaverage s*urface. To do so, we averaged each participants' time-series across runs (number of runs varied between 4 and 12). These participant-average time-series (n=44) were then averaged to create a group-average time-series. The group-average time-series at each vertex was transformed into a group-average BOLD signal. The pRF model was then fit to the group-average BOLD signal to compute group-average pRF maps on the *fsaverage* surface. An example of the pRF model fit to the group-average BOLD signal from a V1 and a V2 vertex is shown in **Figure 2C** and **D**.

7T HCP Retinotopy Dataset

The 7T Human Connectome Project (HCP) Retinotopy Dataset, as described by Benson et al. (2018), contains pRF model solutions for 181 participants. The methods for acquisition and analysis of these data are described in detail in the prior paper. We summarize a few key features here, particularly those that differ from the NYU data. The HCP data were collected at the Center for Magnetic Resonance Research at the University of Minnesota, using a Siemens 7T Magnetom scanner (1.6mm isotropic voxel size) and a 34-channel head coil. The data were processed using specific HCP pipelines, including multimodal surface matching ('*MSMall*') for surface registration, as described by (Glasser et al., 2016). Notably, the publicly available HCP pRF estimates (https://osf.io/bw9ec/) were computed using the *analyzePRF* algorithm (Kay et al., 2013). Here, we recomputed the pRF estimates using *vistasoft* to remove any differences that might arise from differences in pRF software (see Lage-Castellanos et al., 2020; Lerma-Usabiaga et al., 2020). We have made these *vistasoft* pRF estimates publicly available at (https://openneuro.org/datasets/x). These and other differences are summarized in **Table 1**.

	NYU	**HCP**
Participants	44	181
MRI Strength	3 Tesla	7 Tesla
Voxel Size	2mm isotropic	1.6mm isotropic
Stimulus Aperture	Bars	Bars, wedges, and rings
Stimulus Extent	12.4° (radius)	8° (radius)
Stimulus Width	3.1°	2°
Stimulus Update	3 Hz	15 Hz
Pre-processing	fMRIPrep	HCP Pipeline
pRF Model	*vistasoft*	*analyzePRF* for prior public release (reanalyzed with *vistasoft* here)

Table 1. Key differences between the NYU and HCP Retinotopy Datasets.

We implemented the *vistasoft* pRF model on two formats of HCP data. First, on individual participants on the *fsaverage* surface. Using these data, we then computed HCP parameter-median pRF maps. Second, we implemented the pRF model on the group-average time-series on the *fsaverage* surface.

To implement the pRF model on individual HCP participants, we included six scans (2x bar runs, 2x wedge runs, and 2x expanding/contracting ring runs, at 5 mins each; see Benson et al. (2018) for examples of these stimuli). The time-series from these scans were then transformed to BOLD percent signal change. The *vistasoft* pRF model was fit on this BOLD signal. We then computed HCP parmeter-median pRF maps to complete vertex-wise pRF comparisons with the NYU data; we calculated the median x, y, and σ values across all HCP participants and converted these values to polar angle, eccentricity, and pRF size parameters, for each *fsaverage* vertex.

To estimate the HCP group-average pRF maps, all 181 of the participants' time-series on the *fsaverage* surface were averaged together at each vertex independently for each stimulus type (bar, wedge, and ring) to create group-average time-series. These were transformed to BOLD

percent signal change at each vertex. We implemented the *vistasoft* pRF model on these HCP group-averaged BOLD signals to produce group-average pRF maps.

Defining visual area regions-of-interest

Regions-of-interest (ROIs) were defined using the Wang Maximum Probability Atlas (Wang et al., 2015). We identified V1, V2, V3, and hV4. The atlas defined ROI's were used for vertex-wise comparisons between the NYU and HCP Datasets. Additionally, we defined these ROIs by hand on the *fsnative* flatmaps for individual NYU participants using *Neuropythy* v0.11.9 (https://github.com/noahbenson/neuropythy; Benson & Winawer, 2018), following the nomenclature of Wandell, Dumoulin, and Brewer (2007), and of Winawer & Witthoft (2015, 2017) for hV4. The ROI label files, and the code used to draw the ROIs, are made publicly available at OpenNeuro (https://openneuro.org/datasets/x). The hand-labeled V1 ROI was used to compute cortical magnification within the maps.

Defining wedge-ROIs to measure polar-angle meridian asymmetries in cortical magnification

Recently, polar angle meridian asymmetries in V1 cortical magnification have been identified as retinotopic features in the HCP data (Benson et al., 2020). We tested whether these cortical magnification asymmetries are also found in the NYU Retinotopy Dataset. We defined a number of regions-of-interest in V1 corresponding to wedges in the visual field. The wedges were defined using a combination of *Neuropythy* and custom MATLAB code.

The wedges varied in their polar angle center. They were centered on either the left or right horizontal meridian, the upper vertical meridian, or the lower vertical meridian. The polar angle extent of the wedge-width also varied. We tested a range of wedge widths: ±15°, ±25°, ±35°, ±45°, and ±55°. The surface area of the vertices within these wedge-ROIs was summed to find the amount of cortical surface dedicated to processing visual space within these wedges.

PRF polar angle estimates contain measurement noise. Thus, a wedge in the visual field does not typically project to a single enclosed region on the cortex, but rather to a patchy and dispersed set of regions (see Figure 8B in Benson & Winawer, 2018). This complicates the computation of surface area. It is likely that absent measurement noise, the ground truth retinotopic projection of a wedge in the visual field is a single, enclosed region on the cortical surface. Our goal in defining wedge-ROIs was to make reasonable estimates of the surface area of these cortical regions. To do so, we used a procedure similar to that described by (Benson et al., 2020). In brief, we define a cortical ROI corresponding to a wedge in visual space. We do so by generating several sub-ROIs, each of which is constrained to a narrow eccentricity band, and each of which has a width in the polar angle direction derived from the average location of a pool of vertices whose pRF coordinates lie near the wedge boundary in visual space. The eccentricity defined sub-ROIs are then concatenated to yield one full wedge. We describe the specific implementation in more detail below and provide a visualization of the process to define the iso-angle boundary of a 15° wedge extending from the upper vertical meridian in **Figure 3**.

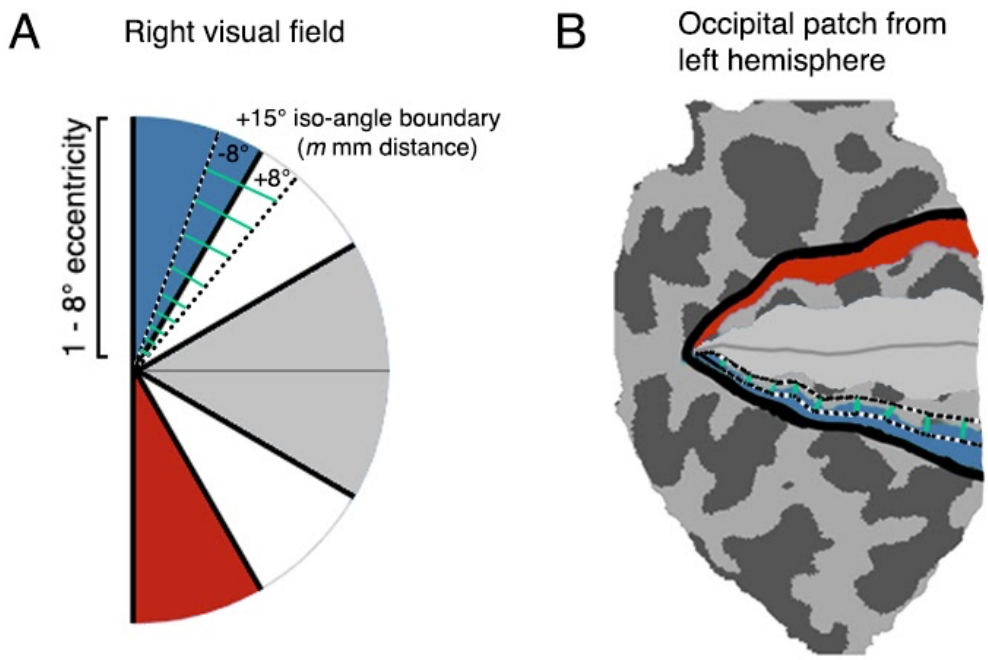

Figure 3. Defining wedge-ROIs and eccentricity band sub-ROIs. The wedge-ROI on the cortex is defined as a wedge in the visual field (A). Because of measurement noise in the retinotopy data, the visual field wedge will not project to a single, enclosed region on the cortex. Instead we find all vertices in the V1 map which lie between 0 and *m* mm distance from the appropriate meridian. The vertices lying on the hand-drawn meridian by definition are at 0 mm from the meridian. To identify the distance m_i of the +15° iso-angle boundary line from the upper vertical meridian in the ith eccentricity bin, we calculate the average cortical distance of the vertices that fall ±8° around the 15° polar angle data. The ±8° boundary is represented by the black and white dotted lines in A and B. The average cortical distance of the +15° iso-angle boundary from the UVM is calculated separately for each of 10 log spaced bins (green lines in A and B). We then define the wedge-ROI mask on the cortex (the blue data in B) as all the vertices between 0 mm distance and m_i mm for each eccentricity sub-region. The cortical surface area within the wedge-ROI mask is summed across the 10 sub-regions. This is repeated for the right hemisphere (left visual field) to define the opposite portion of the UVM wedge. The V1 boundary is outlined in black in (B).

Cortical distances

First, we computed the shortest distance on the cortical surface between each vertex (using Dijkstra's algorithm; Dijkstra, 1959); the same algorithm that powers navigation using google maps) and the appropriate cardinal meridian. For each participant and each hemisphere, we manually defined 3 line-ROIs in V1, for the horizontal, upper, and lower vertical meridians. The cortical representation of the horizontal meridian runs through the approximate middle of V1, the upper vertical meridian representation follows the V1/2 ventral boundary, and the lower vertical meridian representation follows the V1/2 dorsal boundary. The line-ROIs were drawn on the flattened cortical surface using *Neuropythy.* The manual definitions were informed by anatomy (curvature map) and pRF maps (polar angle and eccentricity). These line-ROIs were used to generate 3 *cortical distance maps* for each hemisphere. These cortical distance maps specify the distance of each vertex from each meridian.

Eccentricity boundaries for sub-ROIs

Next, we divided the V1 map into 10 eccentricity bands, log spaced between 1 and 8° of eccentricity. These eccentricity bands were used as sub-ROIs. To ensure that each eccentricity band was a contiguous region, the bands were defined using the retinotopic maps generated by

Bayesian inference (Benson & Winawer, 2018), which combines the participant's vertex-wise pRF estimates with a previously defined retinotopic template to produce a denoised estimate of the visual field. The eccentricity bands were log-spaced in the visual field so that they would be approximately equally spaced in the cortex, as in Benson et al. (2020). The question we were addressing concerned asymmetries in surface area with respect to polar angle, thus, we did not rely on the Bayesian estimates of polar angle. The Bayesian optimization does not explicitly model cortical magnification and thus can induce noise in calculations of an ROI's surface area. Instead, we used *Neuropythy* to implement an optimization that 'cleaned' polar angle pRF fits in V1 for each participant. This minimization seeks to adjust the pRF centers of the vertices as little as possible in order to simultaneously enforce a smooth cortical magnification map, as measured at the individual surface vertices, and correct the field-sign values across V1.

Polar angle boundaries for sub-ROIs

Next, within each eccentricity band, we used the cortical distance maps to compute the average distance of an iso-angle line, representing the outer boundary of the wedge in the visual field, from the center of the wedge (and thus one of the visual field meridians). The iso-angle line was identified by calculating the average distance of the vertices, that had an R^2 above 15%, in the region of cortex 'around' the iso-angle boundary at the defining polar angle value for the wedge-width (i.e., for a 15° wide wedge, this outer iso-angle boundary occurs at 15° in visual space). The vertices 'around' the iso-angle boundary were identified using the cleaned polar angle maps, and were defined as the vertices that fell ±8° polar angle from the iso-angle boundary. We identified the average cortical distance of these vertices to calculate the average cortical distance for the iso-angle line. This was repeated for each eccentricity band.

Closing the sub-ROI

For each eccentricity band, we identified the vertices with a cortical distance between 0mm (i.e., those that fall along a meridian) and the average cortical distance of the iso-angle line. This process is repeated to create a mask for each eccentricity band, for each side of the wedge, and each meridian.

Wedge-ROI

In the final step, we overlay the wedge mask on *cortical surface area maps.* These cortical surface area maps were generated for each participant using *Neuropythy* and specify the cortical surface area (in mm^2) of each vertex on the *fsnative* surface. The cortical surface area is calculated by summing the surface area of the vertices within the wedge mask. The output value is the total surface area of the wedge. For each wedge, the surface areas from left and right hemisphere are summed together to calculate the surface area for the full horizontal meridian, upper vertical meridian, and lower vertical meridian. The upper and lower vertical meridian surface areas are summed to find the surface area of the full vertical meridian.

Results

We present our results across three sections. First, because the NYU Retinotopy Dataset is new, we provide a description of this dataset, including visualizations of pRF maps computed from individual participants and the group-average time-series. Second, we quantify the similarity of NYU and HCP vertex-wise pRF estimates (polar angle, eccentricity, and pRF size) in V1, V2, V3,

and hV4. Third, we report whether the polar angle asymmetries in V1 cortical magnification previously reported in the HCP data (Benson et al., 2020) can be generalized to the NYU data.

NYU Retinotopy Dataset: Individual participants

PRF model solutions were computed for each of the 44 individual participants on the *fsnative* surface. To visualize our data, we mapped our results onto an inflated *fsnative* surface that was then transformed into a sphere, and orthographically projected to a flatmap with data rotated so that the occipital pole aligns to the center of the map (see **Figure 4** for these transformations). Examples of polar angle, eccentricity, and pRF size maps for three example participants (subj004, subj014, and subj042) are illustrated in **Figure 5**. The data are plotted similar to Figure 7 in Benson et al. (2018) for ease of comparison to the HCP retinotopy single-participant data. V1, V2, V3, and hV4 ROIs are drawn in black along the polar angle boundaries. The same pRF maps on inflated meshes are available in **Supplementary Materials Figure S1**. The individual participant maps show clear polar angle, eccentricity, and pRF size representations, and for each participant the maps follow the same broad retinotopic organization, though they differ in detail.

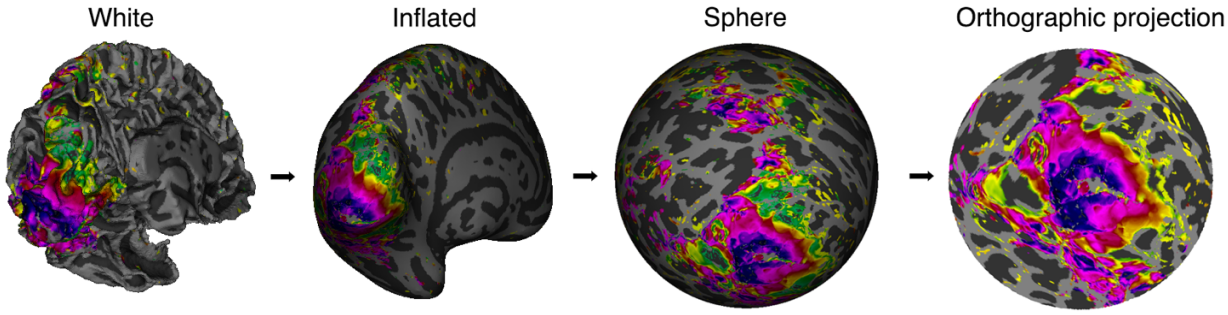

Figure 4. Transform of a left hemisphere cortical surface from white matter mesh through to orthographic projection on a flatmap. The pRF data (in this example, subj004's eccentricity map) are projected onto the *fsnative* surface. The surface is then inflated and smoothed, warped into a sphere, and then rendered as a flatmap with the occipital pole rotated to be at the center of the map.

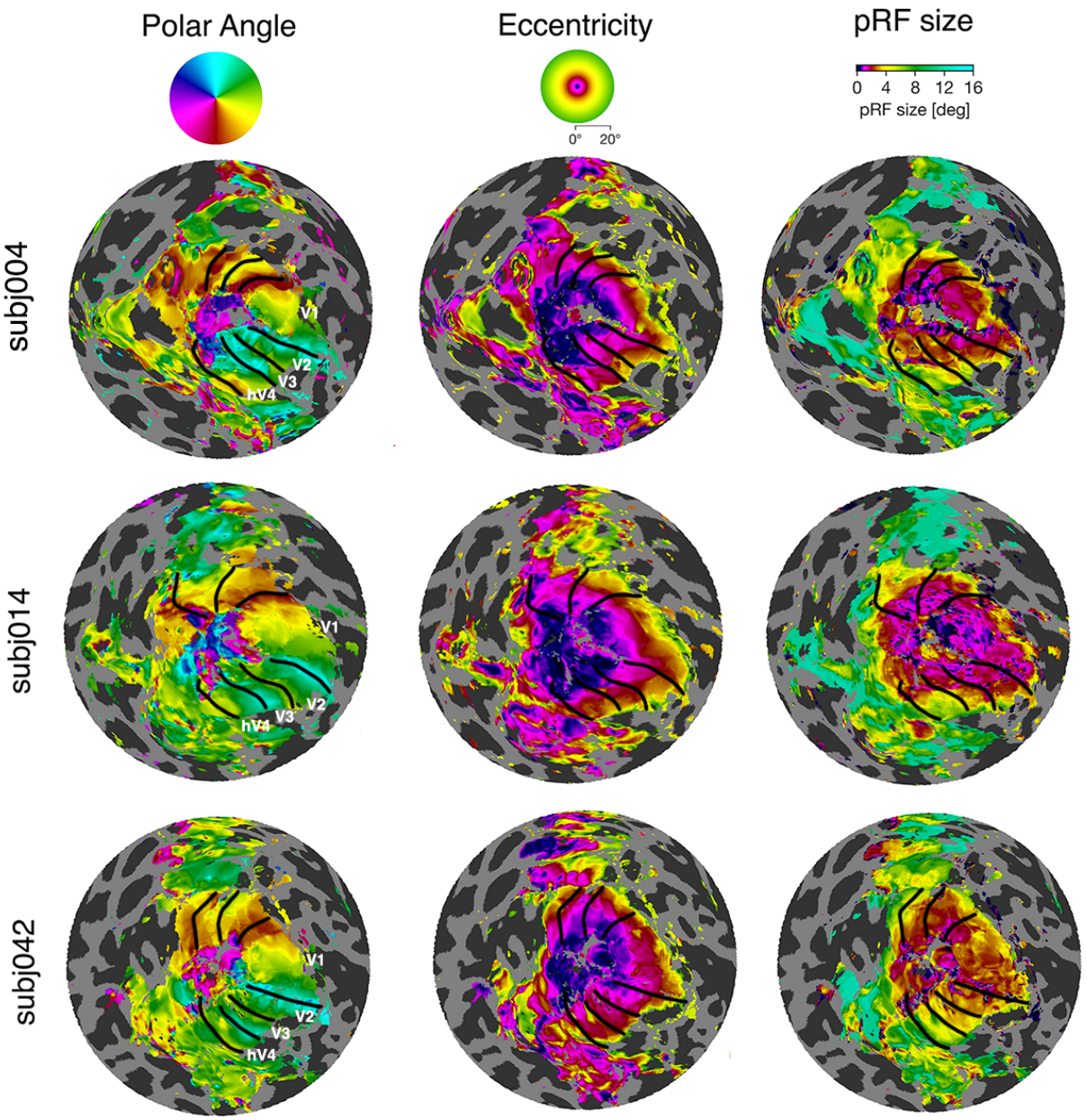

Figure 5. Examples of polar angle, eccentricity, and pRF size maps for three individual participants (subj004, subj014, and subj042). The maps are presented on cortical flat maps on the *fsnative* surface of the left hemisphere. V1, V2, V3, and hV4 ROI boundaries are defined in black.

NYU Retinotopy Dataset: Group-average time-series data

We averaged across 44 participant-averaged time-series on the *fsaverage* surface to create a group-average time-series. The group-average time-series will blur out some features of the fMRI response, particularly in higher-level visual areas where the topography of the maps might not be closely linked to the sulcal patterning. In V1, V2 and V3, many features of the retinotopic maps are preserved after averaging, and the time-averaged data offer a succinct summary of the dataset with a high signal-to-noise ratio. The HCP Retinotopy Dataset also includes the group-averaged time-series data, and hence doing so makes for a useful comparison.

The group-average time-series was transformed to BOLD signal and pRF model solutions were calculated. In **Figure 6**, we present retinotopic maps of the group-averaged data projected onto the inflated *fsaverage* surface for the left and right hemispheres. The visual field representations are located across the occipital cortex and extend along dorsal and ventral regions, as well as frontoparietal cortex (Mackey et al., 2017).

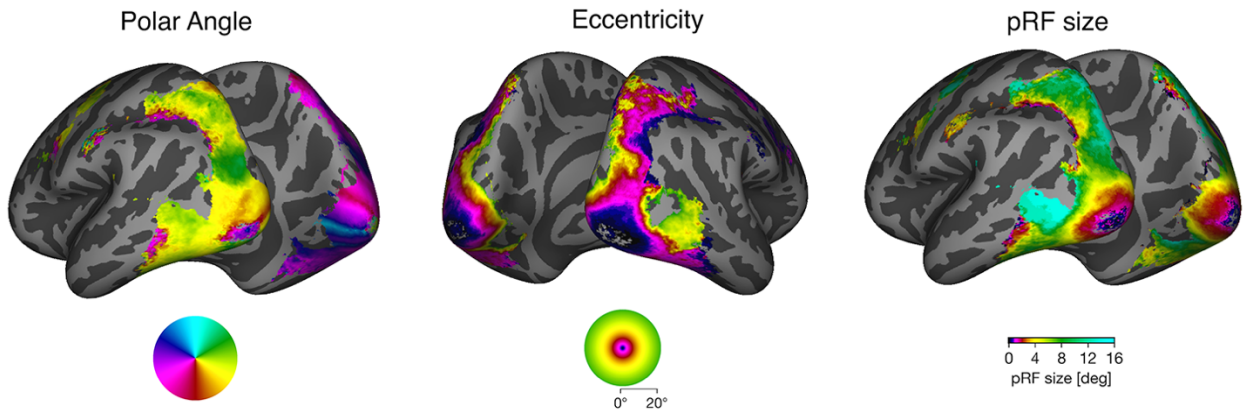

Figure 6. Group-average time-series polar angle, eccentricity, and pRF size maps shown on the left and right hemisphere *fsaverage* inflated surface.

In **Figure 7** we present the group-average polar angle, eccentricity, and pRF size maps for the left and right hemispheres on an *fsaverage* flatmaps, with the occipital pole aligned at the center of the flatmap. The Wang Maximum Probability Atlas (Wang et al., 2015) is overlaid on the retinotopic maps. Examples of these group-average maps with hand drawn V1, V2, V3, and hV4 ROIs are available in **Supplementary Materials Figure S2**. The ROI borders from the Wang Atlas are well-aligned to the polar angle reversals. However, the V1/V2 dorsal boundary appears to be slightly misaligned, falling slightly superior to the red polar angle data. This is common in both the left and right hemisphere. Thus, we suspect that the vertices falling within the Wang V1d ROI contain a small number of vertices from the V2d ROI.

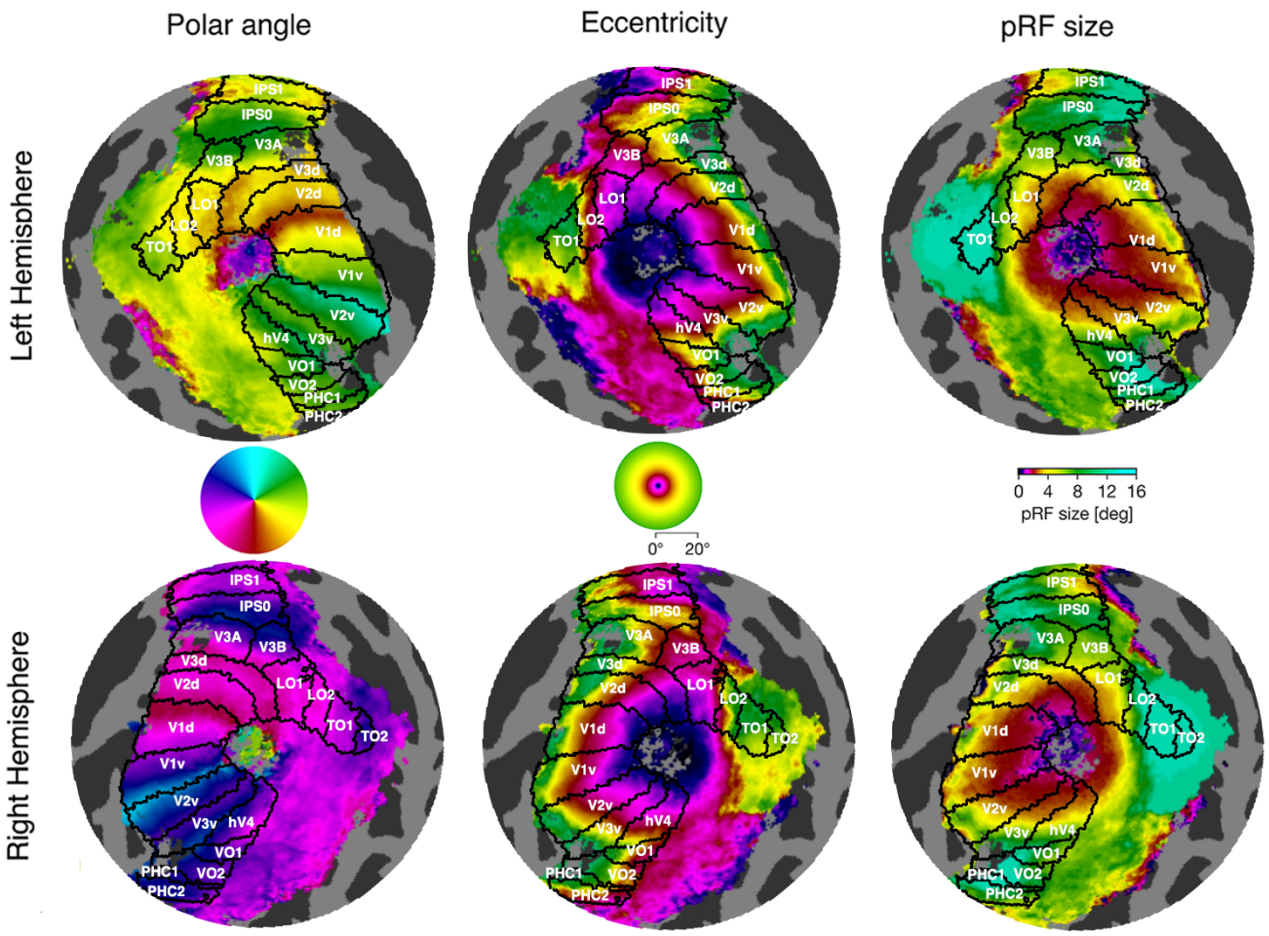

Figure 7. Group-average retinotopic maps shown on the *fsaverage* flatmaps for the left and right hemisphere. The top row presents flatmaps of the left hemisphere (representing the right visual hemifield) and the bottom row presents flatmaps from the right hemisphere (representing the left visual hemifield). Black boundaries are ROI definitions derived from the Wang Maximum Probability Atlas (Wang, Mruczek, Arcaro, & Kastner, 2015).

The maps show the expected retinotopic organization, particularly in the early visual areas; there is a clear polar angle representation with reversals occurring at the ROI boundaries, eccentricity estimates increase with distance from the foveal representation, and pRF sizes increase with eccentricity while scaling to be larger in higher-order areas.

Left hemisphere V1 shows a contralateral representation of the right visual hemifield; the upper bank of the calcarine sulcus represents the lower vertical meridian (red polar angle data). The data show a gradual change in the polar angle representation across the right visual hemifield, through to the lower bank of the calcarine sulcus that represents the upper visual meridian (teal polar angle data). Similarly, the right hemisphere V1 shows a clear contralateral representation of the visual hemifield, with a gradual change in polar angle representation from the lower vertical meridian (red polar angle data), through to the upper vertical meridian (teal polar angle data). Moreover, we can identify clear hemifield representations for the dorsal and ventral regions of V2 and V3 in both hemispheres; both these maps represent quarterfield representations of the contralateral visual field.

There is an artifact in polar angle estimates around the occipital pole, representing the most foveal region of the visual field. These regions show anomalous polar angle representations of the ipsilateral visual field. For example, in **Figure 7**, there is a patch of purple and blue polar angle data around the fovea of the left hemisphere, and there is a patch of yellow and green polar angle data for the right hemisphere. A similar effect was found for individual participants (see **Figure 5**); however, it was not found in the HCP group-average time-series data, perhaps due to the inclusion of rotating wedge stimuli in the HCP experiments. (See **Supplementary Materials S3** for HCP group-average time-series pRF maps from *vistasoft*).

The left and right hemispheres show well-defined eccentricity representations of the visual field, with a shared eccentricity representation between V1, V2, V3, and hV4. The foveal eccentricity representation for these visual field maps begins around the occipital pole (i.e., the foveal confluence) and there is an increasingly peripheral representation of the visual field in increasingly anterior and medial locations.

A similar trend was found for pRF sizes. The left and right hemispheres showed a clear change in pRF size that matched the eccentricity representation; pRF sizes around the occipital pole are small and become larger in increasingly anterior and medial locations away from the occipital pole that represent increasingly eccentric regions of visual space.

Vertex-wise reproducibility of pRF parameters between the NYU and HCP retinotopy data: eccentricity, polar angle, and pRF size

We tested the similarity of polar angle, eccentricity, and pRF size estimates between the NYU and the HCP Retinotopy Datasets. To compare the two datasets, we identified the median pRF parameters at each vertex on the *fsaverage* surface separately for the two datasets. This puts both datasets on a standardized and common surface, making it possible to complete vertex-wise comparisons. For comparison, we group the vertices using ROIs from the Wang Atlas. This provides an automated and unbiased way to bin data in the same manner for the two datasets, even though the atlas-based ROIs only approximately match the visual field maps defined at the level of individual participants. Visualisations of the NYU parameter-median pRF maps, including variance explained maps, are available in **Supplementary Materials Figure S4**.

We compared pRF estimates for vertices that passed an inclusion criteria within each ROI (V1, V2, V3, and hV4). We retained vertices that fell between 0.2° and 6° of eccentricity and survived a 40% variance explained threshold. A vertex was required to meet these criteria for both the NYU and HCP parameter-median data to be included in the analysis. The variance explained threshold removed 10.4% of the vertices within this eccentricity range in the V1-hV4 maps. In **Figure 8**, we present scatterplots comparing vertex-wise NYU and HCP pRF estimates for vertices within V1, V2, V3, and hV4.

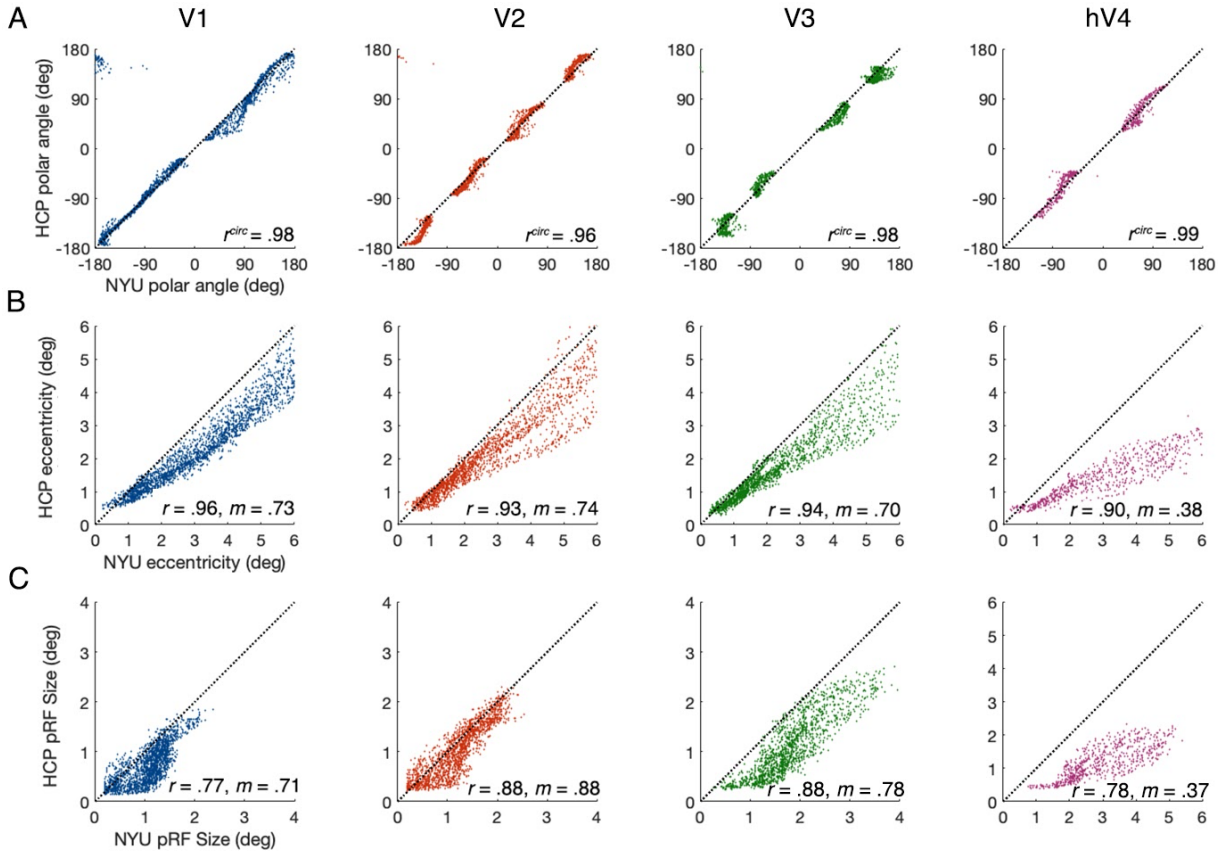

Figure 8. Scatterplots comparing vertex-wise pRF estimates from the NYU and HCP parameter-median data within V1, V2, V3, and hV4. Each datapoint represents an *fsaverage* vertex that has survived a double mask. (**A**) Vertex-wise comparison of polar angle predictions. 0 to +180 degrees polar angle represents the right visual hemifield (with 0 at the upper vertical meridian and -180 the lower vertical meridian), and 0 to -180 degrees polar angle represents the left visual hemifield. (**B**) Vertex-wise comparison of NYU and HCP eccentricity predictions. **(C)** Vertex-wise comparison of NYU and HCP pRF size predictions. Note the different values of the X and Y axis for the hV4 plot in panel C. The black dashed line represents $y = x$. All reported r values are highly significant ($p < .001$).

The polar angle estimates fall close to the identity line and are highly correlated in V1 (circular correlations; $r^{circ} = .98$), V2 ($r^{circ} = .96$), V3 ($r^{circ} = .98$), and hV4 ($r^{circ} = .99$), indicating a close match between NYU and HCP polar angle data (**Figure 8A**). Notably, there are gaps in the data along the polar angle reversals for each visual field map (0° and ±180° for V1 and hV4, and 0°, ±90, and ±180° for V2 and V3). This is likely due to averaging effects, both at the level of individual participants, because voxels pool signals from many neurons, and at the group level, because the borders between visual areas are not in perfect register across participants.

The eccentricity estimates are also highly correlated in V1 (linear correlations; $r = .96$), V2 ($r = .93$), V3 ($r = .94$), and hV4 ($r = .90$) (**Figure 8B**). However, unlike polar angle estimates, there are systematic biases in eccentricity. The NYU eccentricity estimates are generally greater than those from the HCP data in all ROIs. The slopes of the data were similar in V1 ($m = .73$), V2 ($m = .74$), V3 ($m = .70$), and lower in hV4 ($m = .38$). Thus, in V1-V3, for every 1° change in NYU eccentricity, the HCP eccentricity estimate changes by ~0.70°. The larger disagreement between the two datasets in hV4 is addressed in the Discussion.

The pRF size estimates are well correlated in V1 (linear correlations; r = .77), V2 (r = .88), V3 (r = .86), and hV4 (r = .78) (**Figure 8C**). Similar to the eccentricity estimates, there are systematic biases in pRF size: the NYU pRF size estimates are typically larger than those derived from the HCP data. The slopes of the data are similar in V1 (m = .71), V2 (m = .88), V3 (m = .78), and as with eccentricity, lower in hV4 (m = .37).

PRF size vs eccentricity

The previous analysis showed differences between the two datasets in pRF size and eccentricity for the vertex-wise comparisons. Rather than comparing parameters matched by cortical location, we compared parameters matched by eccentricity. Here, we plot the NYU and HCP pRF sizes as a function of eccentricity for V1, V2, V3, and hV4, and fit a linear function through the data. The NYU data (solid lines) and HCP data (dotted lines) show an increase in pRF size as a function of eccentricity and the pRF sizes scale to be larger in sequentially higher order visual areas for each dataset (**Figure 9**). When plotting the pRF sizes relative to eccentricity, the pRF sizes appear more similar between the two datasets than they do when comparing the datasets aligned by location (**Figure 8C**). This is particularly so for V1-V3. Nonetheless, even when plotted as a function of eccentricity, some differences between the two datasets remain. Specifically, the HCP data converge closer to the origin than the NYU data, and the HCP hV4 data are generally smaller than NYU hV4 data.

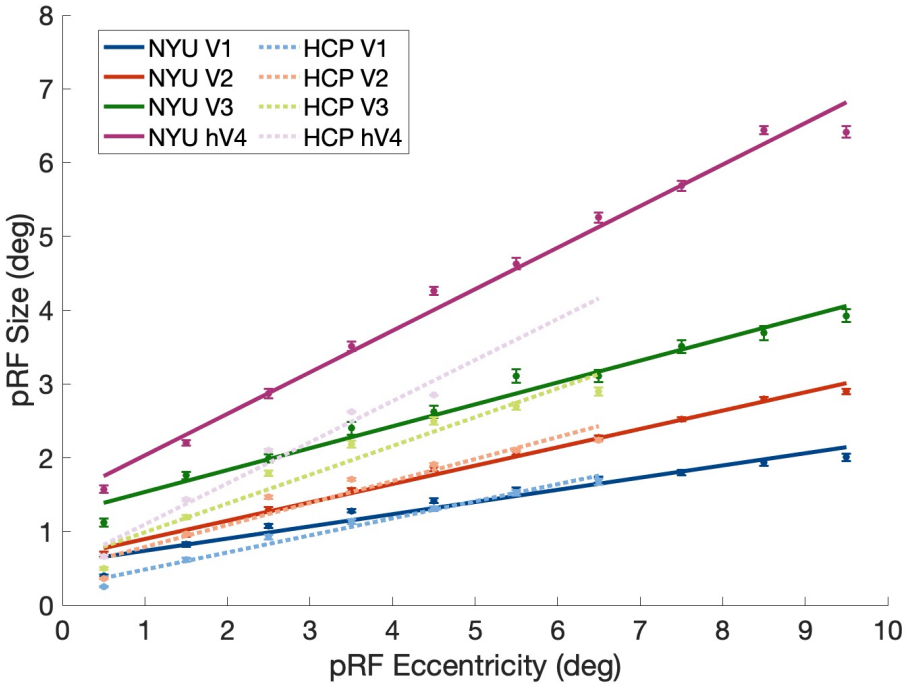

Figure 9. PRF sizes as a function of eccentricity for the NYU (solid lines) and HCP (dashed lines) parameter-median data for V1, V2, V3, and hV4. pRF sizes are binned into 1° eccentricity bins and a linear function is fit to the mean sizes. The NYU data are plotted to 0.5°-9.5° eccentricity, whereas the HCP data are plotted out to 0.5°-6.5° eccentricity due to differences in maximum stimulus extent. Error bars are ±1 SEM (vertices per bin), R^2 threshold = 0.4.

How well do the HCP pRF parameters predict the NYU BOLD signal?

Next, we tested the reproducibility of pRF estimates in *time-series space* rather than *parameter space*. We cannot directly compare the NYU and HCP time-series because the stimuli and length of scans are different. Instead, we tested whether, and how well, a time-series predicted from the x, y, and σ parameters taken from each vertex's HCP pRF estimates explains the NYU BOLD percent signal change.

First, we fit the pRF model on the HCP group-average time-series data to produce pRF parameter estimates on the *fsaverage* surface. We used these parameters to create a new set of predicted time-series by multiplying the NYU stimulus image sequence by the 2D-Gaussians derived from the HCP parameters. These time-series were then convolved with the HRF estimated from the NYU data. For each vertex, we then applied a multiplicative and additive term to best fit the NYU BOLD signal, and calculated the variance explained of the fit for each vertex. This variance explained value provides a quantification of how well a time-series derived from the HCP pRF parameters can explain the NYU data.

In **Figure 10A** we present variance explained maps on the left hemisphere. These maps show the variance explained in the NYU time-series by two models, one fit to the NYU data (direct fit) and one fit to the HCP data (cross-validation). Data are limited to V1, V2, V3, and hV4 as defined by the Wang Atlas, and a maximum of 6° eccentricity. For the NYU pRF fits, the parameters are fit to the same data they are evaluated on, and therefore define a ceiling on how well the data can be fit. In contrast, for the HCP data, the parameters are fit to different data than they are evaluated on (except for the scale factors on the time series), thus these predictions are a form of cross-validation. The HCP-derived predicted time-series provide a good fit to the NYU data in all four visual areas.

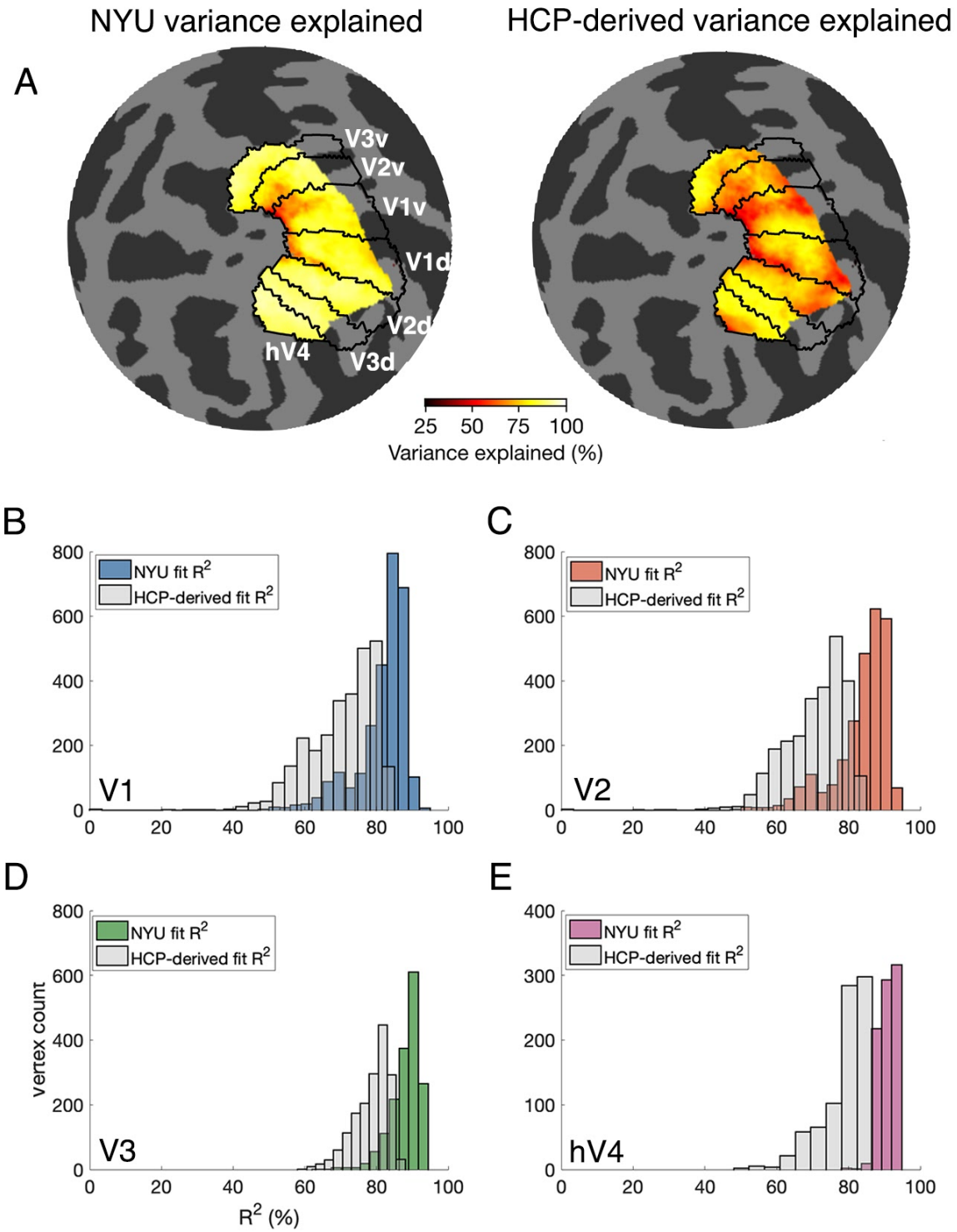

Figure 10. Variance explained maps (left hemisphere) of the NYU and the HCP-derived predicted time-series fit to the NYU BOLD signal and histograms of the variance explained of the NYU and HCP-derived predicted time-series fits in V1, V2, V3, and hV4. **(A)** Flatmaps with the variance explained data in V1-V4 as defined by the Wang atlas. **(B-E)** Histograms of the vertex-wise variance explained (%) of the NYU (solid bars) and HCP-derived (transparent grey bars) model fits. Chance baseline of fitting the recreated predicted time-series to shuffled V1-V4 vertices fell between 1-5%.

The HCP-derived predicted time-series (transparent gray bars) explain over 60% of the variance of the data in the NYU BOLD signal, whereas the NYU predicted time-series (solid bars) explain over 80% of variance (**Figure 10B-E**). These values are similar across V1, V2, V3, and hV4. To calculate an expected variance explained for a null distribution, we applied the same method of fitting predictions from the HCP pRF parameters, except that we shuffled the assignment of pRF parameters to V1-hV4 vertices. For this shuffled distribution, the variance explained in the NYU BOLD signal fell to between 1-5%. Thus, the HCP-derived predicted time-series provide a good explanation for the data, even though the parameters used to build these new predicted time-series come from a different experiment that includes multiple stimulus types.

Polar-angle meridian asymmetries in V1 cortical magnification

Recent work has identified polar angle asymmetries in V1 cortical magnification using the HCP Retinotopy Dataset. More cortical surface area is dedicated to processing the horizontal than vertical visual field meridian (a cortical HVA), and to the lower vertical than the upper vertical meridian (a cortical VMA) (Benson et al., 2020; Silva et al., 2018). The surface area as a function of polar angle aligns with performance on psychophysical tasks (Benson et al., 2018). Here, we tested whether these cortical surface area asymmetries generalize to the NYU Retinotopy Dataset.

For each participant, we calculated cortical surface area of wedges that were centered on the horizontal, upper vertical, and lower vertical visual field meridians (see **Figure 11A** for an example). The wedges increased in width, from ±15° to ±55°, and spanned 1° to 8° of eccentricity.

We were able to confirm the cortical HVA and VMA in our data. In **Figure 11B** and **11C**, we present the mean cortical surface area measurements for the wedges. In agreement with Benson et al. (2020), there is more cortical surface dedicated to processing the horizontal meridian than the vertical meridian (**Figure 11B**). Similarly, there is more cortical surface area dedicated to processing the lower vertical meridian than the upper vertical meridian (**Figure 11C**).

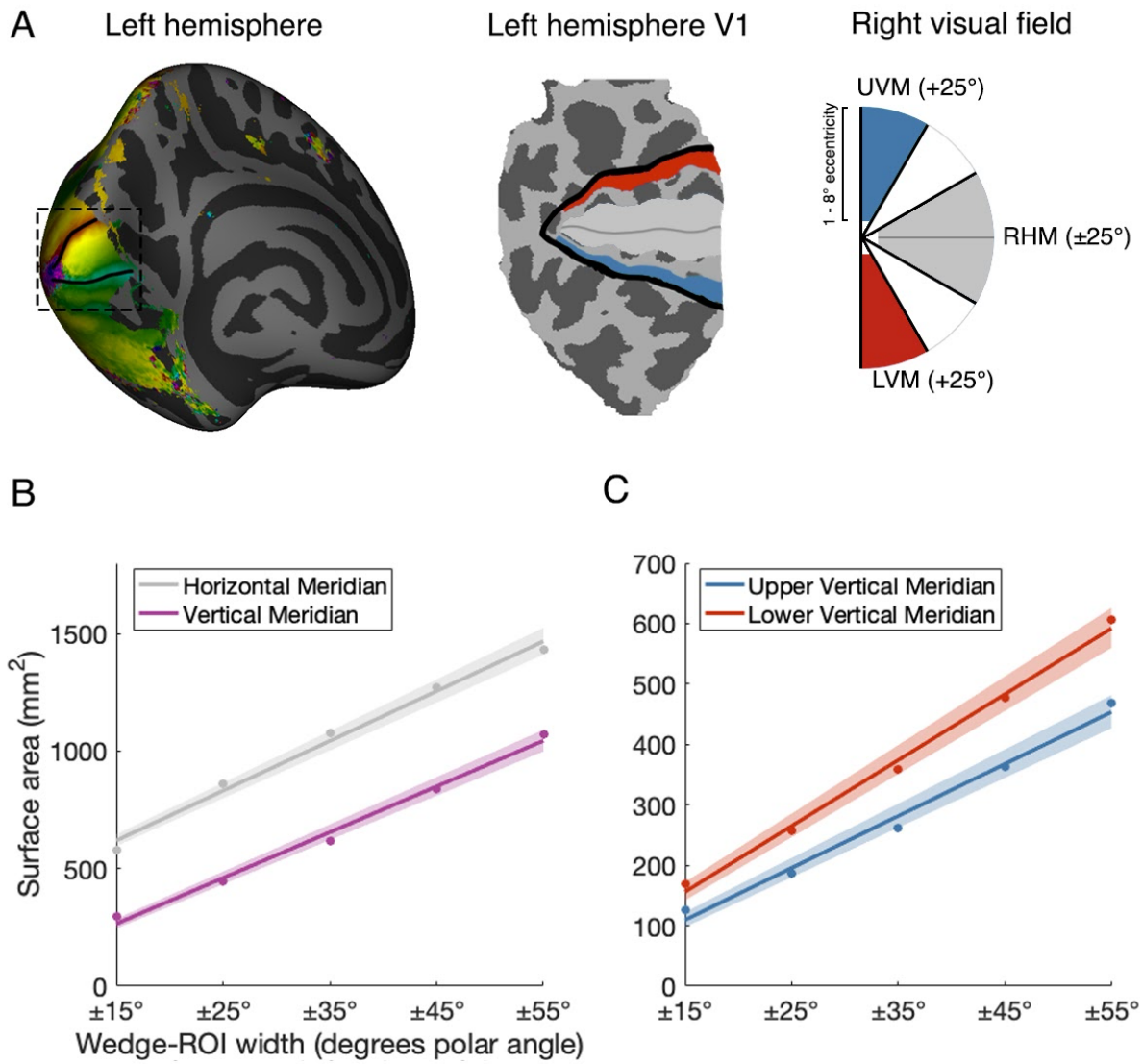

Figure 11. Examples of wedges in the visual field and their representation on the cortical surface of V1, and group-mean cortical surface area measurements plotted as a function of wedge width. **(A)** An inflated left hemisphere with a polar angle map. The black borders show the boundaries of V1. The right visual field is mapped onto the left hemisphere of V1, and the wedges are centered on the upper vertical meridian, right horizontal meridian, and lower vertical meridian. The mapping of the wedge onto the cortical surface area is shown on the flattened left hemisphere V1. We sum the cortical surface area of the vertices within the colored wedge to find the total surface area of each wedge. The horizontal meridian wedge is ±25° whereas the upper vertical meridian and lower vertical meridian are +25° (not to scale) because the full upper vertical meridian and lower vertical meridian wedge is formed by summing cortical space from the left *and* right hemisphere. **(B)** Cortical surface area measurements for wedges centered on the horizontal and vertical meridians, plotted as a function of wedge-width. **(C)** Cortical surface area measurements for wedges centered on the upper and lower vertical meridians, plotted as a function of wedge-width. Colored lines represent the average of 1000 bootstrapped linear fits to the data (colored data points). The shaded error bar represents the 68% bootstrapped CI of the linear fit to the data.

Next, we calculated HVA and VMA asymmetry indices for each participant and each wedge. The HVA asymmetry index was calculated as the difference in surface area between the vertical meridian and the horizontal meridian, divided by the mean of the two, multiplied by 100. The VMA asymmetry index was calculated as the difference in surface area between the upper vertical meridian and the lower vertical meridian, divided by the mean of the two, multiplied by

100. Thus, a positive HVA or VMA asymmetry indicates an effect in line with the behavioral HVA or VMA and a larger index represents a stronger asymmetry.

The HVA asymmetry (**Figure 12A**) was around 65% for a ±15° wedge and the asymmetry decreased with increasing wedge-width. Thus, near the meridians, there is almost twice as much surface area dedicated to processing the horizontal compared to the vertical visual field meridian. The VMA (**Figure 12B**) was smaller, though still substantial, with around a 30% asymmetry for a ±15° wedge, and again, the asymmetry decreased with increasing wedge-width. For both the HVA and VMA, as the wedge width increases and the asymmetry decreases, the confidence interval increases. Hence, the most robust asymmetries for wedge-ROIs are close to the meridians. HVA and VMA asymmetries for incremental ±5° wedge are reported in **Supplementary Materials Figure S5**.

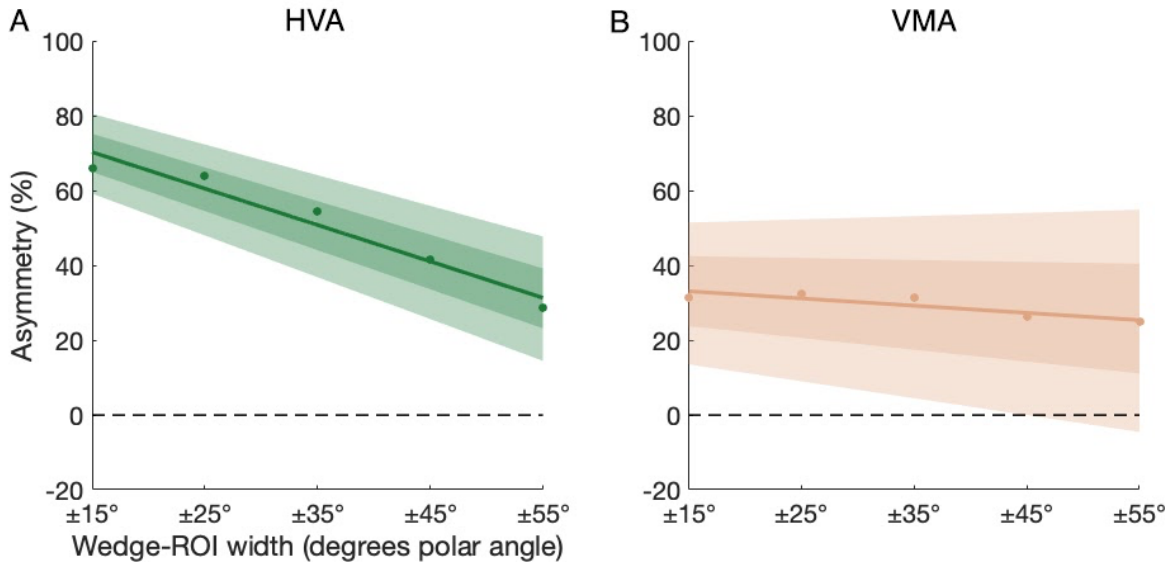

Figure 12. Group-mean HVA and VMA indices plotted as a function of wedge width. Green and red lines represent the average of 1000 bootstrapped linear fits to the mean values (colored data points) at each wedge width. The light shaded error bar represents the 95% bootstrapped CI and the dark shaded error bar represents the 68% bootstrapped CI.

Discussion

Here, we have described a new, publicly available dataset; the NYU Retinotopy Dataset. We then tested the cross-dataset reproducibility between the NYU and HCP Retinotopy Datasets. Although these two datasets differ in many aspects, our goal was to examine how similar they are in terms of the retinotopic properties of human V1 - hV4. First, we tested the reproducibility of vertex-wise pRF estimates in V1, V2, V3, and hV4. Second, we tested the similarity of the HCP and NYU pRF estimates in time-series space. Both of these analyses found a high degree of similarity between the two datasets. Third, we compared the two datasets in terms of polar angle meridian asymmetries in V1 cortical magnification. The NYU data showed the same pattern previously reported for the HCP data: more cortical surface area was dedicated to the horizontal than the vertical visual field meridian, and to the lower than the upper vertical visual field meridian.

Benefits of the NYU Retinotopy Dataset and Data Availability

The NYU Retinotopy Dataset consists of a large set of publicly available retinotopy data and can serve as a complement to the HCP 7T Retinotopy Dataset. All of the HCP data were acquired and processed in a similar manner, thus any potential limits or biases in one participant's data may apply to all of them. The same is true for the NYU data. For this reason, no matter how large one dataset is, it is important to have multiple, independent datasets to validate findings.

The NYU Retinotopy Dataset is publicly available for download (https://openneuro.org/datasets/x) and contains comprehensive data for all 44 participants. This includes anatomical images, raw and preprocessed functional images on the *fsnative* and *fsaverage* surfaces, *vistasoft* pRF model outputs on *fsnative* and *fsaverage* surfaces, and hand drawn V1, V2, V3, and hV4 ROIs for individual participants. Further, the organization and structure for the dataset adheres to BIDS (Brain Imaging Data Structure; (Gorgolewski et al., 2016). This means that the dataset is accessible, follows a clear and intuitive structure, and can be readily reanalyzed by others using scripts in which the inputs adhere to BIDS conventions. For example, it should be relatively simple to reanalyze the NYU Retinotopy Dataset with a different version of *fMRIPrep* or implement a different pRF model.

Next, we provide hand-drawn ROI labels for V1, V2, V3, and hV4 for each participant, facilitating further analyses of these areas by other researchers. We do not provide explicit ROIs for other regions, instead we provide *Jupyter Notebook* code and instructions for users to hand-define additional ROIs in this or other datasets using *Neuropythy*. The data were acquired for the whole brain, enabling investigation of maps in a variety of findings outside occipital cortex, such as the recent studies of retinotopy in hippocampus (Silson et al., 2021), cerrelebelum (van Es et al., 2019), and parietal and frontal cortices (Mackey et al., 2017). The data can also be used to address questions of pRF shape, such as center surround organization (Zuiderbaan et al., 2012) or ellipticity (Silson et al., 2018).

As we have implemented the *vistasoft* pRF model on the HCP data, we also provide a new release of the *vistasoft* pRF model solutions for all 181 HCP participants on the *fsaverage* surface. This complements the published pRF solutions from the same data using different software.

Vertex-wise polar angle, eccentricity, and pRF size estimates are well-correlated between datasets

First, we tested the vertex-wise similarity of NYU and HCP polar angle, eccentricity, and pRF size estimates using the parameter-median data. Overall, the pRF estimates were strongly correlated between the two datasets.

Vertex-wise polar angle estimates were almost perfectly correlated between the two datasets. Both the NYU and HCP data produced similar polar angle estimates at each individual vertex, and this was consistent across visual areas. Previously, a within-session split-half analysis of the HCP Retinotopy Dataset identified polar angle estimates as the most internally reliable pRF parameter (Benson et al., 2018). Other work has shown that the polar angle estimates are consistent for the same participants across sessions and across aperture types (van Dijk et al., 2016). Here, we extend these analyses by showing that at the group level, the polar angle maps are highly similar between datasets.

Similarly, vertex-wise eccentricity estimates were strongly correlated, however, the two sets of estimates differed by a scale factor (~.75 in V1-V3 and ~0.4 in hV4), with the NYU eccentricity estimates higher than those from the HCP data.

A scale factor difference in eccentricity between the datasets could arise for multiple reasons. First, it could be due to an anatomical shift of one dataset relative to the other. Specifically, one could account for the observed 3:4 ratio in eccentricity estimates by a translation along the posterior-anterior axis of about 4 mm, assuming the cortical magnification function of Horton & Hoyt, (1991). Differences in the registration methods used during preprocessing might result in such a small, but systematic, shift in alignment: A cortical curvature-based alignment is used for the NYU data and a multimodal "MSMAll" alignment is used for the HCP data (Glasser et al., 2016). A second possibility is calibration errors in the stimulus size. In each dataset, it was assumed that all participants viewed the stimulus from a fixed distance (83.5 cm for NYU experiment and 101.5 cm for HCP experiment). Inevitably, there are small variations in the viewing distance and thus stimulus size due to differences in the positioning of each participant in the scanner. This has been noted in the methods of the HCP retinotopy study (Benson et al., 2018). Errors in stimulus size estimation would result in a scale factor difference in the eccentricity but not polar angle data, as is observed in our study. Third, differences in eccentricity estimates might be linked to differences in the pRF stimuli. The stimuli differed in temporal frequency (3 vs 15 Hz stimulus image update), width (3.1° vs 2°), and maximal extent (12.4° vs 8° radius). Differences in estimated eccentricity possibly arise from non-linearities in the neural response that are not modeled in the 2-D Gaussian pRF model. Finally, any of these three factors might combine to give rise to the observed differences.

Like eccentricity, pRF sizes were well-correlated between the two datasets, with a systematic bias towards larger pRFs in the NYU data. This bias was found in V1 to hV4. The simplest explanation is that the pRF size difference is caused by the same factors that cause the eccentricity difference. Supporting this, when pRF size is compared to eccentricity within a dataset, the differences between datasets are greatly reduced. For example, for both datasets, at 4° eccentricity, the sizes in V1 are about 1° and in V3 about 2°. Nonetheless, some differences remain. In particular, the HCP sizes were smaller than the NYU sizes at central eccentricities (below 3°) but the sizes are relatively similar to the NYU data in more peripheral eccentricities (beyond 3° eccentricity). Such differences in pRF size may arise from the use of a rotating wedge stimulus in the HCP experiments, but not the NYU experiments. The rotating wedge scales in size with eccentricity and may be useful for estimating small pRF sizes near the fovea.

Differences between the NYU and HCP datasets in hV4

The hV4 map properties differ more between the two datasets than the V1, V2, and V3 map properties. Several factors may contribute to this difference: First, in addition to differences in stimulus design, the two datasets differ in voxel size. The NYU voxels are about two times greater in volume. Greater volume should result in larger pRF sizes. PRF size depends on both neural receptive field size and the scatter of neural receptive field centers across the visual field (Dumoulin & Wandell, 2008). Larger voxels contain more neurons and hence more scatter. Neural receptive field scatter will likely have a large effect on estimated pRF size for voxels in small visual areas. If a visual area is small (such as hV4, which is about half the size of the V1-V3 maps) then the neurons within a single voxel will sample a relatively large portion of the visual field, hence there will be more scatter per voxel. Second, because the two datasets were aligned to

the template surface using different algorithms, there is likely to be some degree of systematic spatial warping between the two datasets. A spatial warping will cause a relatively larger misalignment between small visual areas than large visual areas. This could explain the shallow slope in the hV4 vertex-wise scatter plots of both eccentricity and pRF size. Third, we compared map properties between the two datasets using visual field map ROIs defined by an anatomical template, rather than ROIs identified in individual subjects based on functional data. Anatomical atlases tend to be most accurate for early visual areas, especially V1 (Benson et al., 2012), but also V2 and V3 (Benson et al., 2014; Benson & Winawer, 2018). They tend to be less accurate for higher visual areas such as hV4 (Wang et al., 2015). As a result, the hV4 comparisons are likely to include more data from other neighboring areas than the V1, V2, and V3 comparisons.

Fitting the predicted time-series based on the HCP pRF parameter estimates to the NYU BOLD percent signal change

The relation between pRF parameters and the BOLD signal is nonlinear. Depending on the stimulus design, a small change in a pRF parameter can result in a large change in the predicted time-series, and conversely, a large change in a pRF parameter can result in a small change in the predicted time-series (Lerma-Usabiaga et al., 2020; Zeidman et al., 2018). Therefore, it is informative to compare datasets in the time-series space as a complement to the parameter space.

To compare the datasets in time-series space, we fit a predicted time-series that was built using the HCP pRF estimates (that were multiplied by the NYU stimulus sequence and convolved with the NYU HRF) to the NYU BOLD percent signal change. Notably, these HCP pRF estimates were initially derived using multiple stimulus types (bars, wedges, and rings) whereas the NYU pRF estimates were derived from bar stimuli alone. This recreated predicted time-series provided an excellent fit to the NYU data in V1, V2, V3 and hV4, explaining 60-85% of the variance in the NYU BOLD signal. This is close to the maximal explainable variance that was derived from directly fitting the NYU BOLD signal, which explained 80-95% of variance. Thus, the pRF estimates for the NYU and HCP data were highly similar in time-series space.

Implications of the similarities and differences between the NYU and HCP Datasets

The pattern of similarities and differences between the two datasets is important for quantitative interpretation of retinotopic data, especially with respect to comparisons between data from different sites. The polar angle data are highly consistent between the NYU and HCP experiments, with circular correlation coefficients above 95% in each of V1, V2, V3, and hV4. Polar angle is especially important for identification of visual area boundaries, thus different studies are likely to be able to achieve close agreement in delineation of visual field maps. Why do the polar angle estimates show such close agreement? First, polar angle estimates are immune to differences in scale of stimulus coordinates. Second, they are likely to be insensitive to differences in voxel size. Third, pRF model predictions, given typical stimulation sequences, are sharply tuned to polar angle, enabling precise estimates of this parameter (Lage-Castellanos et al., 2020; Lerma-Usabiaga et al., 2020).

The small but systematic differences in eccentricity and pRF size indicate that a measure of tolerance is required when generalizing from one dataset to another. For example, the anatomically defined retinotopic template from Benson and Winawer (2018) was generated using

HCP data. If the template is applied to a different dataset without constraints from functional measures, there might be a small-scale factor error in the eccentricity estimates in V1, V2, and V3, and a larger error in hV4 and other higher visual areas. The fact that the parameter estimates are so strongly correlated between the datasets indicates that random noise plays a minimal role in generating the differences in eccentricity and pRF size. In turn, this suggests that it should be feasible to resolve the modest between-dataset differences, for example, with a corrective spatial warping or a calibration using a standardized stimulus and anatomical landmarks.

Polar angle meridian asymmetries in V1 cortical magnification are reproducible across datasets

Reports of *performance fields* show that visual performance on a range of tasks changes as a function of polar angle (Abrams et al., 2012; Baldwin et al., 2012; Barbot et al., 2021; Cameron et al., 2002; Carrasco et al., 2001; Carrasco et al., 2002; Corbett & Carrasco, 2011; Fortenbaugh et al., 2015; Fuller et al., 2008; Greenwood et al., 2017; Himmelberg et al., 2020; Levine & McAnany, 2005; Lundh et al., 1983; Montaser-Kouhsari & Carrasco, 2009; Pointer & Hess, 1989; Regan & Beverley, 1983; Rijsdijk et al., 1980; Robson & Graham, 1981; Silva et al., 2008; Talgar & Carrasco, 2002; Virsu & Rovamo, 1979). Previous fMRI studies have reported similar polar angle asymmetries in V1 cortical magnification (Benson et al., 2020; Silva et al., 2018) and BOLD amplitude (Liu et al., 2006). In parallel to behavior, more cortical space is dedicated to processing the horizontal than vertical visual field meridian (i.e., a cortical HVA). Likewise, there is more cortical space dedicated to the lower vertical than upper vertical visual field meridian (i.e., a cortical VMA). We tested whether these polar angle asymmetries are also found in the NYU data.

The HVA was identified in the NYU data; around a 65% HVA asymmetry index for a ±15° wedge. Thus, there is almost twice as much cortical space along the horizontal than vertical visual field meridian. The HVA became progressively weaker with increasing wedge-width. This indicates that the cortical HVA is strongest along the meridians themselves. This measurement qualitatively and quantitatively corresponds to the cortical HVA identified by Benson et al. (2020). Likewise, the VMA was identified in the NYU data; around a 30% VMA asymmetry index for a ±15° wedge. Thus, there is more surface area dedicated to the lower than upper visual field meridian. This is similar to the cortical VMA identified by Benson et al. (2020), however, one discrepancy is that in the NYU data, the VMA asymmetry gradually decreased with wedge-width, whereas in the HCP data, the VMA decreased more rapidly.

Notably, our cortical HVA and VMA measurements are commensurate with recent psychophysical data, both of which show a larger HVA than VMA. For contrast sensitivity, the HVA is approximately 60% (similar to the ~65% cortical HVA reported here) whereas the VMA is weaker at approximately 20% (similar to the ~30% cortical HVA reported here) (Himmelberg et al., 2020). For acuity, the HVA is approximately 40% and the VMA is approximately 20% (Barbot et al., 2021). Our cortical magnification measurements match these perceptual measurements; in fact, these perceptual measurements come from a subsample of the participants included in the present study. Recent implementations of computational models have shown that polar angle asymmetries in photoreceptor and retinal ganglion cell sampling density only account for a small portion of *performance field* asymmetries, and that the sampling of the visual field as a function of polar angle is more asymmetric in cortex than in the retina (Kupers et al., 2019, 2020). We are currently developing a computational model to assess the extent to which these cortical asymmetries can account for perceptual performance field asymmetries in contrast sensitivity.

Overall, the HVA is strong and clear, and these asymmetries in cortical geometry can be measured robustly in independent datasets. Qualitatively, the VMA was reproduced between the two datasets, corroborating that this cortical asymmetry exists. However, there were small differences in the detailed characterization of the VMA between the two datasets. The asymmetry between the upper and lower meridian declined faster with angular distance from the vertical meridian in the HCP dataset compared to the NYU dataset. Such differences may arise from subtle differences in our analysis compared to Benson et al. (2020). The horizontal, upper vertical, and lower vertical visual field boundaries on the *cortical distance maps* were defined by hand in the NYU data; this meant that we only accounted for vertical meridian surface area within V1, whereas Benson et al. (2020) accounted for vertical meridian surface area in both V1 and V2. Further, the NYU data used cleaned polar angle data, whereas Benson et al. (2020) used raw polar angle data. Thus, it is not surprising that small differences in results arise from small differences in analysis. Nonetheless, despite some quantitative differences, the overall pattern of more surface area for horizontal than vertical visual field meridian representations, and for lower than upper vertical visual field meridian representations, holds across datasets and analysis methods.

Retinotopic maps are reproducible

Identifying and understanding retinotopic maps is a central aim of visual neuroscience. We endeavor to understand how the visual brain is organized into multiple visual areas, identify the functional roles of these areas, and understand how they unite to make sense of the influx of sensory information that ultimately gives rise to visual perception. This is no small feat, and if newly identified retinotopic areas and features are to be considered generalizable across the human population, they must be subject to tests of validity and reliability to ensure that findings are robust and generalizable across independent datasets.

Previous studies have assessed reproducibility of retinotopic maps via different tests of validity. PRF estimates are reported to have good intersession reliability. Specifically, they are consistent across time in the same observers who were measured twice in the same scanner (Lage-Castellanos et al., 2020; van Dijk et al., 2016). This is supported by split-half analysis in the HCP retinotopy data, in which each participant's functional scans were split into first and second halves, and pRF parameters were estimated twice (Benson et al., 2018). Likewise, pRF estimates have been shown to be similar across subjects when measured with the same stimuli, in the same scanner, and analyzed from the same data; the HCP data analyzed as split half by subject showed that each subgroup of half the subjects had very similar average pRF maps (Benson et al., 2018). Next, it has been shown that pRFs are reproducible when the same subjects are tested with different stimulus apertures and carrier images, using the same scanner and same software (van Dijk et al., 2016). Finally, computational validity is the ability of software to reproduce the *correct result* for simulated ground truth test data (irrespective of whether it is the *same* answer), and this has been assessed using a recent validation framework tested against different pRF modelling software (Lerma-Usabiaga et al., 2020). Here, we have assessed retinotopic reproducibility in a different way from prior studies. We assessed reliability of retinotopic maps at the group level, by comparing two independent datasets that differed in their stimulus design, participants, MRI hardware, fMRI protocol, and preprocessing pipeline. These experimental differences are typical for data collected from different labs. We have shown that many retinotopic properties in human V1 to hV4 can be reliably reproduced, even with these experimental differences.

Recently, there has been considerable interest in the reproducibility of scientific results in the biomedical sciences (Ioannidis, 2005), with much attention drawn to results in psychology (Open Science Collaboration, 2015) and neuroimaging (Poldrack et al., 2017). For example, reports show that reproducibility is poor for many task-based fMRI experiments (Elliott et al., 2020). This may reflect limitations in the kind of experiments tested, as some studies show higher reproducibility than others (Kragel et al., 2021). Similarly, the same data analyzed by different groups often led to different results and conclusions (Botvinik-Nezer et al., 2020).

Our data show that retinotopic maps are reliable and reproducible between independent datasets that have been acquired using different fMRI protocols, measured using different stimuli, and undergone different preprocessing. We suggest that this is because the methods underlying the measurement of retinotopic maps circumvent many of the issues involved in irreproducibility (see Poldrack et al. (2017) for review). PRF estimates are computed using an explicit computational model of the fMRI response and this model is defined in terms of input parameters (Dumoulin & Wandell, 2008; Wandell & Winawer, 2015). These input parameters are grounded in solid theory of neural visual receptive fields; We formalize a pRF as a 2D-Gaussian and this is based on the established physiological structure of neural receptive fields in the visual cortex (Hubel & Wiesel, 1968). Thus, the fMRI response is modelled using a quantitative characterization of neural activity. Using this powerful computational modeling approach, retinotopic maps can be reliably measured, and integrated, across different neural measurements (Wandell et al., 2015).

Conclusion

We have tested the cross-dataset reproducibility of retinotopic properties by comparing two independent datasets that differ in many aspects. We have reported that polar angle, eccentricity, and pRF size estimates are well-correlated between the two datasets, albeit with systematically larger eccentricity and pRF size estimates in the NYU data. These systematic differences in eccentricity and pRF size might be linked to small differences in anatomical alignment methods or viewing distance. Differences in pRF size may also arise from differences in voxel size and stimulus aperture. Next, we identified polar angle asymmetries in V1 cortical magnification similar to those found in the HCP data. There was more cortical surface area dedicated to the horizontal than vertical visual field meridian, and to the lower than upper vertical visual field meridian, and these asymmetries decreased gradually with increasing distance from the meridians. The pattern and strength of these asymmetries was similar to those reported from previous behavioural measurements, supporting a link between brain and behavior. Overall, we have shown that we can reliably describe retinotopic properties in human V1 to hV4 from two datasets that differ in many respects, and we highlight the importance of the cross-dataset validation of new retinotopic findings to ensure that they can be generalized across the human population. The NYU Retinotopy Dataset can serve as a benchmark for testing hypotheses about the organization of human visual cortex and for comparison to the 7T HCP Retinotopy Dataset.

Author contributions

M.M.H, J.W.K, M.C, and J.W conceived the experiments. M.M.H, N.C.B, and J.W performed the experiments. M.M.H, J.W.K, & J.W analyzed the data. M.M.H and J.W wrote the paper with feedback from J.W.K, N.C.B, D.G.P, and M.C.

Acknowledgements
Some of the NYU datasets were originally collected for other projects for which retinotopy was just one component. We thank Billy Broderick, Serra Favila, Iris Groen, and Eline Kupers for contributing their datasets to this paper.

References

Abrams, J., Nizam, A., & Carrasco, M. (2012). Isoeccentric locations are not equivalent: the extent of the vertical meridian asymmetry. *Vision Research*, *52*(1), 70–78. https://doi.org/10.1016/j.visres.2011.10.016

Baldwin, A. S., Meese, T. S., & Baker, D. H. (2012). The attenuation surface for contrast sensitivity has the form of a witch's hat within the central visual field. *Journal of Vision*, *12*(23). https://doi.org/10.1167/12.11.23

Barbot, A., Xue, S., & Carrasco, M. (2021). Asymmetries in visual acuity around the visual field. *Journal of Vision*, *21*(1), 2. https://doi.org/10.1167/jov.21.1.2

Benson, N. C., Butt, O. H., Brainard, D. H., & Aguirre, G. K. (2014). Correction of Distortion in Flattened Representations of the Cortical Surface Allows Prediction of V1-V3 Functional Organization from Anatomy. *PLoS Computational Biology*, *10*(3). https://doi.org/10.1371/journal.pcbi.1003538

Benson, N. C., Butt, O. H., Datta, R., Radoeva, P. D., Brainard, D. H., & Aguirre, G. K. (2012). The retinotopic organization of striate cortex is well predicted by surface topology. *Current Biology: CB*, *22*(21), 2081–2085. https://doi.org/10.1016/j.cub.2012.09.014

Benson, N. C., Jamison, K. W., Arcaro, M. J., Vu, A. T., Glasser, M. F., Coalson, T. S., Van Essen, D. C., Yacoub, E., Ugurbil, K., Winawer, J., & Kay, K. (2018). The Human Connectome Project 7 Tesla retinotopy dataset: Description and population receptive field analysis. *Journal of Vision*, *18*(13), 1–22. https://doi.org/10.1167/18.13.23

Benson, N. C., Kupers, E. R., Barbot, A., Carrasco, M., & Winawer, J. (2020). Cortical Magnification in Human Visual Cortex Parallels Task Performance around the Visual Field. In *Cold Spring Harbor Laboratory* (p. 2020.08.26.268383). https://doi.org/10.1101/2020.08.26.268383

Benson, N. C., & Winawer, J. (2018). Bayesian analysis of retinotopic maps. *eLife*, *7*, 1–29. https://doi.org/10.7554/eLife.40224

Binda, P., Thomas, J. M., Boynton, G. M., & Fine, I. (2013). Minimizing biases in estimating the reorganization of human visual areas with BOLD retinotopic mapping. *Journal of Vision*, *13*(7), 13. https://doi.org/10.1167/13.7.13.doi

Botvinik-Nezer, R., Holzmeister, F., Camerer, C. F., Dreber, A., Huber, J., Johannesson, M., Kirchler, M., Iwanir, R., Mumford, J. A., Adcock, R. A., Avesani, P., Baczkowski, B. M., Bajracharya, A., Bakst, L., Ball, S., Barilari, M., Bault, N., Beaton, D., Beitner, J., … Schonberg, T. (2020). Variability in the analysis of a single neuroimaging dataset by many teams. *Nature*, *582*(7810), 84–88. https://doi.org/10.1038/s41586-020-2314-9

Cameron, E. L., Tai, J. C., & Carrasco, M. (2002). Covert attention affects the psychometric function of contrast sensitivity. *Vision Research*, *42*(8), 949–967. https://doi.org/10.1016/s0042-6989(02)00039-1

Carrasco, M., Talgar, C. P., & Cameron, E. L. (2001). Characterizing visual performance fields: effects of transient covert attention, spatial frequency, eccentricity, task and set size. *Spatial Vision*, *15*(1), 61–75. https://doi.org/10.1163/15685680152692015

Carrasco, M., Williams, P. E., & Yeshurun, Y. (2002). Covert attention increases spatial resolution with or without masks: Support for signal enhancement. *Journal of Vision*, *2*(6), 1351–1365. https://doi.org/10.1167/2.6.4

Corbett, J. E., & Carrasco, M. (2011). Visual performance fields: frames of reference. *PloS One*, *6*(9), e24470. https://doi.org/10.1371/journal.pone.0024470

Dale, A. M., Fischl, B., & Sereno, M. I. (1999). Cortical surface-based analysis: I. Segmentation and surface reconstruction. *NeuroImage*. https://doi.org/10.1006/nimg.1998.0395

DeYoe, E. A., Bandettini, P., Neitz, J., Miller, D., & Winans, P. (1994). Functional magnetic resonance imaging (FMRI) of the human brain. *Journal of Neuroscience Methods*, *54*(2), 171–187. https://doi.org/10.1016/0165-0270(94)90191-0

Dijkstra, E. W. (1959). A note on two problems in connexion with graphs. *Numerische Mathematik*, *1*(1), 269–271. https://doi.org/10.1007/bf01386390

Dumoulin, S. O., & Wandell, B. A. (2008). Population receptive field estimates in human visual cortex. *NeuroImage*, *39*(2), 647–660.

Elliott, M. L., Knodt, A. R., Ireland, D., Morris, M. L., Poulton, R., Ramrakha, S., Sison, M. L., Moffitt, T. E., Caspi, A., & Hariri, A. R. (2020). What Is the Test-Retest Reliability of Common Task-Functional MRI Measures? New Empirical Evidence and a Meta-Analysis. *Psychological Science*, *31*(7), 792–806. https://doi.org/10.1177/0956797620916786

Engel, S. A., Rumelhart, D. E., Wandell, B. A., Glover, G. H., Eduardo-Jose, C., & Shadlen, M. N. (1994). fMRI of human visual cortex. *Nature*, *369*(June), 525.

Esteban, O., Markiewicz, C. J., Blair, R. W., Moodie, C. A., Isik, A. I., Erramuzpe, A., Kent, J. D., Goncalves, M., DuPre, E., Snyder, M., Oya, H., Ghosh, S. S., Wright, J., Durnez, J., Poldrack, R. A., & Gorgolewski, K. J. (2019). fMRIPrep: a robust preprocessing pipeline for functional MRI. *Nature Methods*, *16*(1), 111–116. https://doi.org/10.1038/s41592-018-0235-4

Feinberg, D. A., Moeller, S., Smith, S. M., Auerbach, E., Ramanna, S., Glasser, M. F., Miller, K. L., Ugurbil, K., & Yacoub, E. (2010). Multiplexed echo planar imaging for sub-second whole brain fmri and fast diffusion imaging. *PloS One*, *5*(12). https://doi.org/10.1371/journal.pone.0015710

Fortenbaugh, F. C., Silver, M. A., & Robertson, L. C. (2015). Individual differences in visual field shape modulate the effects of attention on the lower visual field advantage in crowding. *Journal of Vision*, *15*(2). https://doi.org/10.1167/15.2.19

Friston, K. J., Fletcher, P., Josephs, O., Holmes, A., Rugg, M. D., & Turner, R. (1998). Event-Related fMRI: Characterizing Differential Responses. *NeuroImage*, *7*(1), 30–40. https://doi.org/10.1006/nimg.1997.0306

Fuller, S., Rodriguez, R. Z., & Carrasco, M. (2008). Apparent contrast differs across the vertical meridian: Visual and attentional factors. *Journal of Vision*, *8*(1), 1–16. https://doi.org/10.1167/8.1.16

Glasser, M. F., Coalson, T. S., Robinson, E. C., Hacker, C. D., Harwell, J., Yacoub, E., Ugurbil, K., Andersson, J., Beckmann, C. F., Jenkinson, M., Smith, S. M., & Van Essen, D. C. (2016). A multi-modal parcellation of human cerebral cortex. *Nature*, *536*(7615), 171–178. https://doi.org/10.1038/nature18933

Gorgolewski, K., Burns, C. D., Madison, C., Clark, D., Halchenko, Y. O., Waskom, M. L., & Ghosh, S. S. (2011). Nipype: A flexible, lightweight and extensible neuroimaging data processing framework in Python. *Frontiers in Neuroinformatics*, *5*(August). https://doi.org/10.3389/fninf.2011.00013

Gorgolewski, K. J., Auer, T., Calhoun, V. D., Craddock, R. C., Das, S., Duff, E. P., Flandin, G., Ghosh, S. S., Glatard, T., Halchenko, Y. O., Handwerker, D. A., Hanke, M., Keator, D., Li, X., Michael, Z., Maumet, C., Nichols, B. N., Nichols, T. E., Pellman, J., … Poldrack, R. A. (2016). The brain imaging data structure, a format for organizing and describing outputs of neuroimaging experiments. *Scientific Data*, *3*(160044). https://doi.org/10.1038/sdata.2016.44

Greenwood, J. A., Szinte, M., Sayim, B., & Cavanagh, P. (2017). Variations in crowding, saccadic precision, and spatial localization reveal the shared topology of spatial vision. *Proceedings of the National Academy of Sciences of the United States of America*, *114*(17). https://doi.org/10.1073/pnas.1615504114

Harvey, B. M., & Dumoulin, S. O. (2011). The Relationship between Cortical Magnification Factor and Population Receptive Field Size in Human Visual Cortex: Constancies in Cortical Architecture. *Journal of Neuroscience*, *31*(38), 13604–13612. https://doi.org/10.1523/JNEUROSCI.2572-11.2011

Himmelberg, M. M., Winawer, J., & Carrasco, M. (2020). Stimulus-dependent contrast sensitivity asymmetries around the visual field. *Journal of Vision*, *20*(9), 18. https://doi.org/10.1167/jov.20.9.18

Horton, J. C., & Hoyt, W. F. (1991). The representation of the visual field in human striate cortex. A revision of the classic Holmes map. *Archives of Ophthalmology*, *109*(6), 816–824. https://doi.org/10.1001/archopht.1991.01080060080030

Hubel, D. H., & Wiesel, T. N. (1968). Receptive fields and the functional architecture of monkey striate cortex. *The Journal of Physiology*, *195*(1), 215–243. https://doi.org/10.1113/jphysiol.1968.sp008455

Ioannidis, J. P. A. (2005). Why most published research findings are false. *PLoS Medicine*, *2*(8), e124. https://doi.org/10.1371/journal.pmed.0020124

Kay, K. N., Winawer, J., Mezer, A., & Wandell, B. A. (2013). Compressive spatial summation in human visual cortex. *Journal of Neurophysiology*, *110*(2), 481–494. https://doi.org/10.1152/jn.00105.2013

Kleiner, M., Brainard, D. H., Pelli, D. G., Broussard, C., Wolf, T., & Niehorster, D. (2007). What's new in Psychtoolbox-3? *Perception*.

Kragel, P. A., Han, X., Kraynak, T. E., Gianaros, P. J., & Wager, T. D. (2021). Functional MRI Can Be Highly Reliable, but It Depends on What You Measure: A Commentary on Elliott et al. (2020). *Psychological Science*, 0956797621989730. https://doi.org/10.1177/0956797621989730

Kriegeskorte, N. (2008). Representational similarity analysis – connecting the branches of systems neuroscience. *Frontiers in Systems Neuroscience*, *2*(4), 1–28. https://doi.org/10.3389/neuro.06.004.2008

Kupers, E. R., Benson, N. C., Carrasco, M., & Winawer, J. (2020). Radial asymmetries around the visual field: From retina to cortex to behavior. *bioRxiv*. https://doi.org/10.1101/2020.10.20.347492

Kupers, E. R., Carrasco, M., & Winawer, J. (2019). Modeling visual performance differences 'around' the visual field: A computational observer approach. *PLoS Computational Biology*, *15*(5), e1007063. https://doi.org/10.1371/journal.pcbi.1007063

Kurzawski, J. W., Mikellidou, K., Morrone, M. C., & Pestilli, F. (2020). The visual white matter connecting human area prostriata and the thalamus is retinotopically organized. *Brain Structure & Function*, *225*(6), 1839–1853. https://doi.org/10.1007/s00429-020-02096-5

Lage-Castellanos, A., Valente, G., Senden, M., & De Martino, F. (2020). Investigating the Reliability of Population Receptive Field Size Estimates Using fMRI. *Frontiers in Neuroscience*, *14*, 825. https://doi.org/10.3389/fnins.2020.00825

Lerma-Usabiaga, G., Benson, N., Winawer, J., & Wandell, B. A. (2020). A validation framework for neuroimaging software: The case of population receptive fields. *PLoS Computational Biology*, *16*(6), 1–18. https://doi.org/10.1371/journal.pcbi.1007924

Levine, M. W., & McAnany, J. J. (2005). The relative capabilities of the upper and lower visual hemifields. *Vision Research*, *45*(21), 2820–2830. https://doi.org/10.1016/j.visres.2005.04.001

Liu, T., Heeger, D. J., & Carrasco, M. (2006). Neural correlates of the visual vertical meridian asymmetry. *Journal of Vision*, *6*(11), 1294–1306. https://doi.org/10.1167/6.11.12

Lundh, B. L., Lennerstrand, G., & Derefeldt, G. (1983). Central and peripheral normal contrast sensitivty for static and dynamic sinusoidal gratings. *Acta Ophthalmologica*, *61*(2), 171–182. https://doi.org/10.1111/j.1755-3768.1983.tb01410.x

Mackey, W. E., Winawer, J., & Curtis, C. E. (2017). Visual field map clusters in human frontoparietal cortex. *eLife*, *6*, 1–23. https://doi.org/10.7554/eLife.22974

Montaser-Kouhsari, L., & Carrasco, M. (2009). Perceptual asymmetries are preserved in short-term memory tasks. *Attention, Perception & Psychophysics*, *71*(8), 1782–1792. https://doi.org/10.3758/APP.71.8.1782

Open Science Collaboration. (2015). Estimating the reproducibility of psychological science. *Science*, *349*(6251). https://doi.org/10.1126/science.aac4716

Pointer, J. S., & Hess, R. F. (1989). The contrast sensitivity gradient across the human visual field: With emphasis on the low spatial frequency range. *Vision Research*, *29*(9), 1133–1151. https://doi.org/10.1016/0042-6989(89)90061-8

Poldrack, R. A., Baker, C. I., Durnez, J., Gorgolewski, K. J., Matthews, P. M., Munafò, M. R., Nichols, T. E., Poline, J.-B., Vul, E., & Yarkoni, T. (2017). Scanning the horizon: towards transparent and reproducible neuroimaging research. *Nature Reviews. Neuroscience*, *18*(2), 115–126. https://doi.org/10.1038/nrn.2016.167

Regan, D., & Beverley, K. I. (1983). Visual fields described by contrast sensitivity, by acuity, and by relative sensitivity to different orientations. *Investigative Ophthalmology & Visual Science*, *24*(6), 753–759. https://www.ncbi.nlm.nih.gov/pubmed/6853102

Rijsdijk, J. P., Kroon, J. N., & van der Wildt, G. J. (1980). Contrast sensitivity as a function of position on the retina. *Vision Research*, *20*(3), 235–241. https://doi.org/10.1016/0042-6989(80)90108-X

Robson, J. G., & Graham, N. (1981). Probability summation and regional variation in contrast sensitivity across the visual field. *Vision Research*, *21*(3), 409–418. https://doi.org/10.1016/0042-6989(81)90169-3

Schira, M. M., Tyler, C. W., Breakspear, M., & Spehar, B. (2009). The foveal confluence in human visual cortex. *Journal of Neuroscience*, *29*(28), 9050–9058. https://doi.org/10.1523/JNEUROSCI.1760-09.2009

Senden, M., Reithler, J., Gijsen, S., & Goebel, R. (2014). Evaluating population receptive field estimation frameworks in terms of robustness and reproducibility. *PloS One*, *9*(12), 1–30. https://doi.org/10.1371/journal.pone.0114054

Sereno, M. I., Dale, A. M., Reppas, J. B., Kwong, K. K., Belliveau, J. W., Brady, T. J., Rosen, B. R., & Tootell, R. B. H. (1995). Borders of multiple visual areas in humans revealed by functional magnetic resonance imaging. *Science*. https://doi.org/10.1126/science.7754376

Silson, E. H., Reynolds, R. C., Kravitz, D. J., & Baker, C. I. (2018). Differential Sampling of Visual Space in Ventral and Dorsal Early Visual Cortex. In *The Journal of Neuroscience* (Vol. 38, Issue 9, pp. 2294–2303). https://doi.org/10.1523/jneurosci.2717-17.2018

Silson, E. H., Zeidman, P., Knapen, T., & Baker, C. I. (2021). Representation of Contralateral Visual Space in the Human Hippocampus. *The Journal of Neuroscience: The Official Journal of the Society for Neuroscience*, *41*(11), 2382–2392. https://doi.org/10.1523/JNEUROSCI.1990-20.2020

Silva, M. F., Brascamp, J. W., Ferreira, S., Castelo-Branco, M., Dumoulin, S. O., & Harvey, B. M. (2018). Radial asymmetries in population receptive field size and cortical magnification factor in early visual cortex. *NeuroImage*, *167*, 41–52. https://doi.org/10.1016/j.neuroimage.2017.11.021

Silva, M. F., Maia-Lopes, S., Mateus, C., Guerreiro, M., Sampaio, J., Faria, P., & Castelo-

Branco, M. (2008). Retinal and cortical patterns of spatial anisotropy in contrast sensitivity tasks. *Vision Research*, *48*(1), 127–135. https://doi.org/10.1016/j.visres.2007.10.018

Szinte, M., & Knapen, T. (2020). Visual Organization of the Default Network. *Cerebral Cortex* , *30*(6), 3518–3527. https://doi.org/10.1093/cercor/bhz323

Talgar, C. P., & Carrasco, M. (2002). Vertical meridian asymmetry in spatial resolution: Visual and attentional factors. *Psychonomic Bulletin & Review*, *9*, 714–722. https://doi.org/10.3758/BF03196326

van Dijk, J. A., de Haas, B., Moutsiana, C., & Schwarzkopf, D. S. (2016). Intersession reliability of population receptive field estimates. *NeuroImage*, *143*, 293–303. https://doi.org/10.1016/j.neuroimage.2016.09.013

van Es, D. M., van der Zwaag, W., & Knapen, T. (2019). Topographic Maps of Visual Space in the Human Cerebellum. *Current Biology: CB*, *29*(10), 1689–1694.e3. https://doi.org/10.1016/j.cub.2019.04.012

Virsu, V., & Rovamo, J. (1979). Visual resolution, contrast sensitivity, and the cortical magnification factor. *Experimental Brain Research. Experimentelle Hirnforschung. Experimentation Cerebrale*, *37*, 475–494. https://doi.org/10.1007/BF00236818

Wandell, B. A., Dumoulin, S. O., & Brewer, A. A. (2007). Visual field maps in human cortex. *Neuron*, *56*(2), 366–383. https://doi.org/10.1016/j.neuron.2007.10.012

Wandell, B. A., & Winawer, J. (2015). Computational neuroimaging and population receptive fields. *Trends in Cognitive Sciences*, *19*(6), 349–357. https://doi.org/10.1016/j.tics.2015.03.009

Wandell, B. A., Winawer, J., & Kay, K. N. (2015). *Computational Modeling of Responses in Human Visual Cortex* (Vol. 1, pp. 651–659). Elsevier Inc. https://doi.org/10.1016/B978-0-12-397025-1.00347-X

Wang, L., Mruczek, R. E. B., Arcaro, M. J., & Kastner, S. (2015). Probabilistic maps of visual topography in human cortex. *Cerebral Cortex* , *25*(10), 3911–3931. https://doi.org/10.1093/cercor/bhu277

Winawer, J., & Witthoft, N. (2015). Human V4 and ventral occipital retinotopic maps. *Visual Neuroscience*, *32*, E020. https://doi.org/10.1017/S0952523815000176

Winawer, J., & Witthoft, N. (2017). Identification of the ventral occipital visual field maps in the human brain. *F1000Research*, *6*, 1526. https://doi.org/10.12688/f1000research.12364.1

Worsley, K. J., Liao, C. H., Aston, J., Petre, V., Duncan, G. H., Morales, F., & Evans, A. C. (2002). A general statistical analysis for fMRI data. *NeuroImage*, *15*(1), 1–15. https://doi.org/10.1006/nimg.2001.0933

Xu, J., Moeller, S., Auerbach, E. J., Strupp, J., Smith, S. M., Feinberg, D. A., Yacoub, E., & Uğurbil, K. (2013). Evaluation of slice accelerations using multiband echo planar imaging at 3T. *NeuroImage*, *83*, 991–1001. https://doi.org/10.1016/j.neuroimage.2013.07.055

Zeidman, P., Silson, E. H., Schwarzkopf, D. S., Baker, C. I., & Penny, W. (2018). Bayesian population receptive field modelling. *NeuroImage*, *180*(September 2017), 173–187. https://doi.org/10.1016/j.neuroimage.2017.09.008

Zhang, Y., Brady, M., & Smith, S. (2001). Segmentation of brain MR images through a hidden Markov random field model and the expectation-maximization algorithm. *IEEE Transactions on Medical Imaging*, *20*(1), 45–57. https://doi.org/10.1109/42.906424

Zuiderbaan, W., Harvey, B. M., & Dumoulin, S. O. (2012). Modeling center-surround configurations in population receptive fields using fMRI. *Journal of Vision*, *12*(3), 10. https://doi.org/10.1167/12.3.10

Supplementary Materials

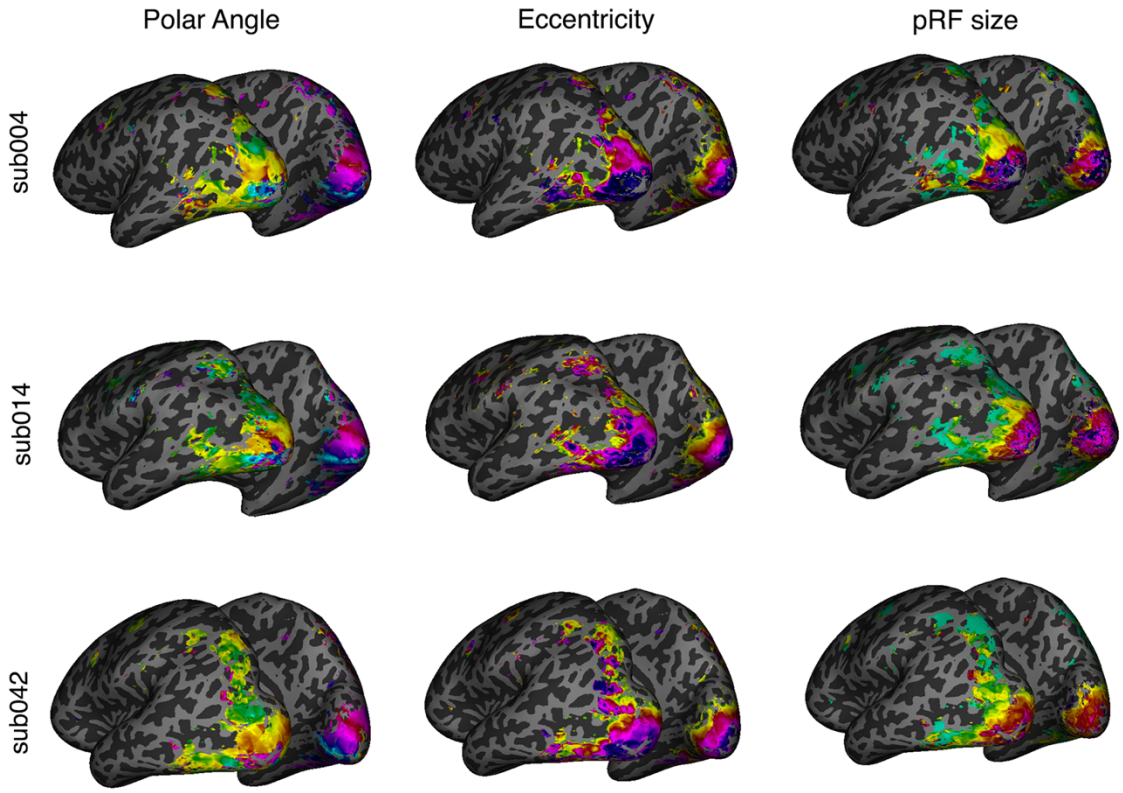

Figure S1. Examples of retinotopic maps for three individual participants (subj004, subj014, and subj042) projected onto the inflated *fsnative* surface.

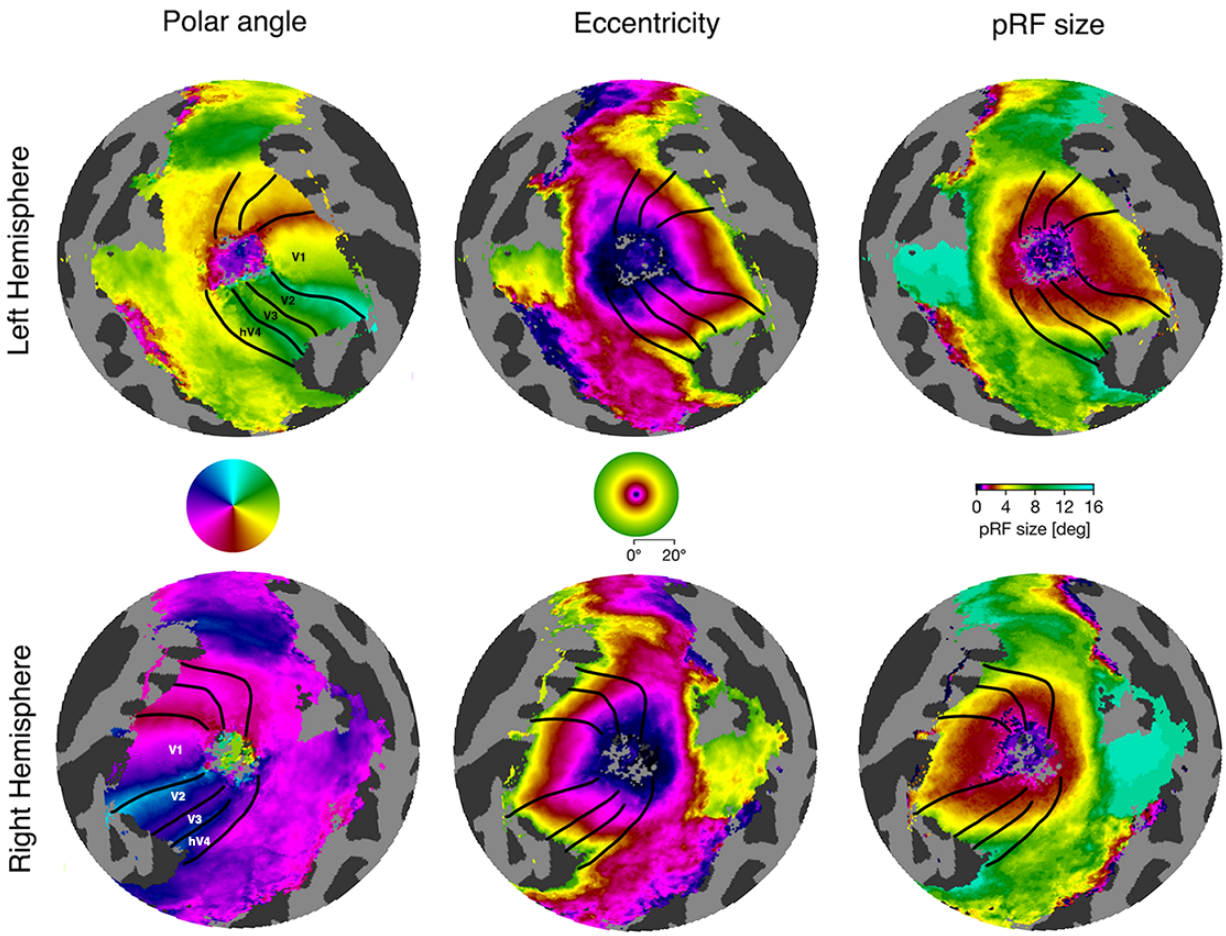

Figure S2. Retinotopic maps for the NYU group-average time-series retinotopic projected on the *fsaverage* cortical flat map for the left and right hemispheres. Black boundaries are used to define the V1, V2, V3, and hV4 ROIs.

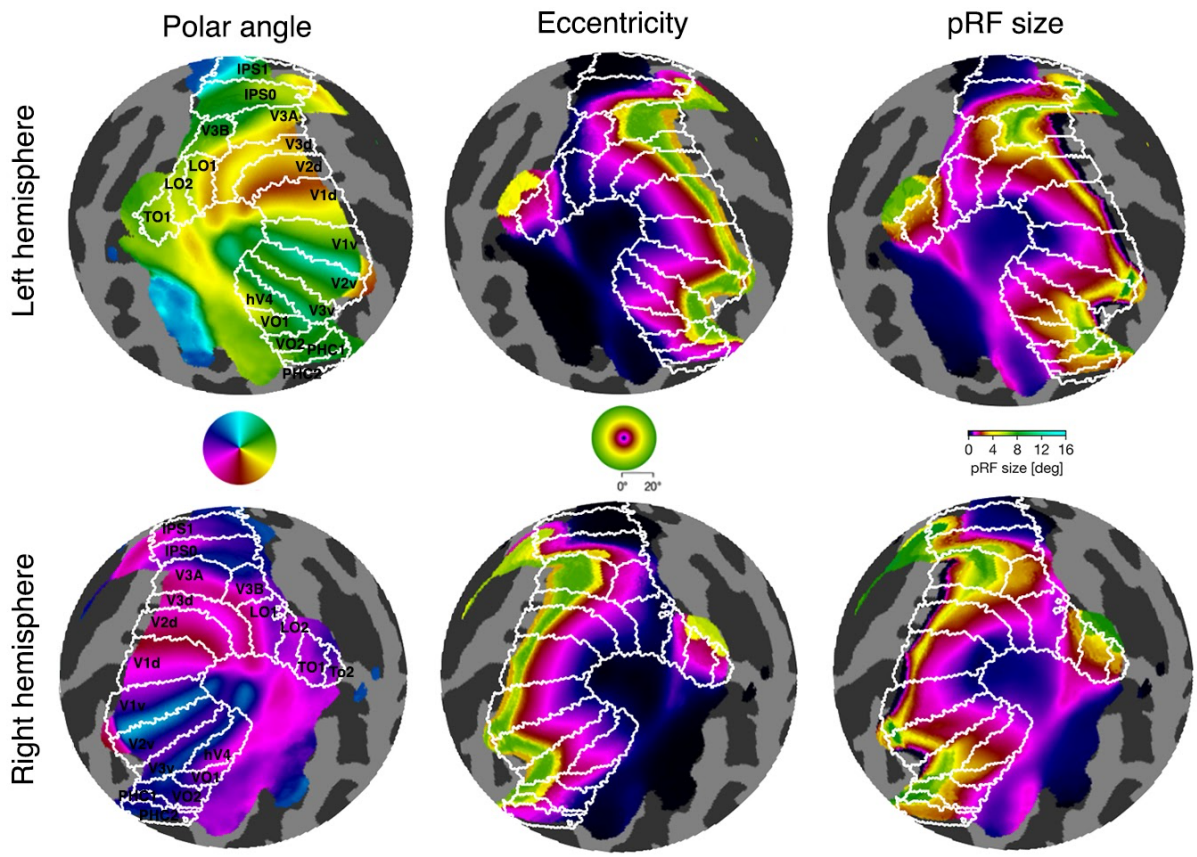

Figure S3. Retinotopic maps for the HCP group-average time-series projected on *fsaverage* flatmaps for the left and right hemisphere. White boundaries specify ROIs derived from the Wang Maximum Probability Atlas.

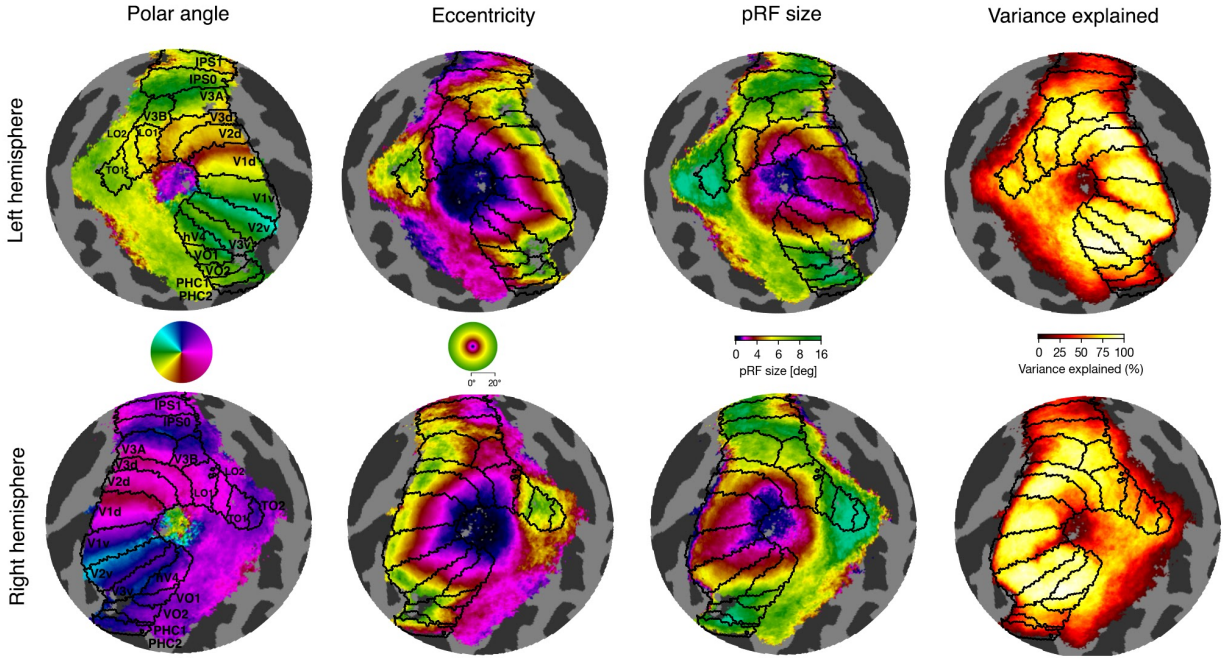

Figure S4. Retinotopic maps and the variance explained map for the NYU parameter-median data projected onto *fsaverage* flatmaps for the left and right hemisphere.

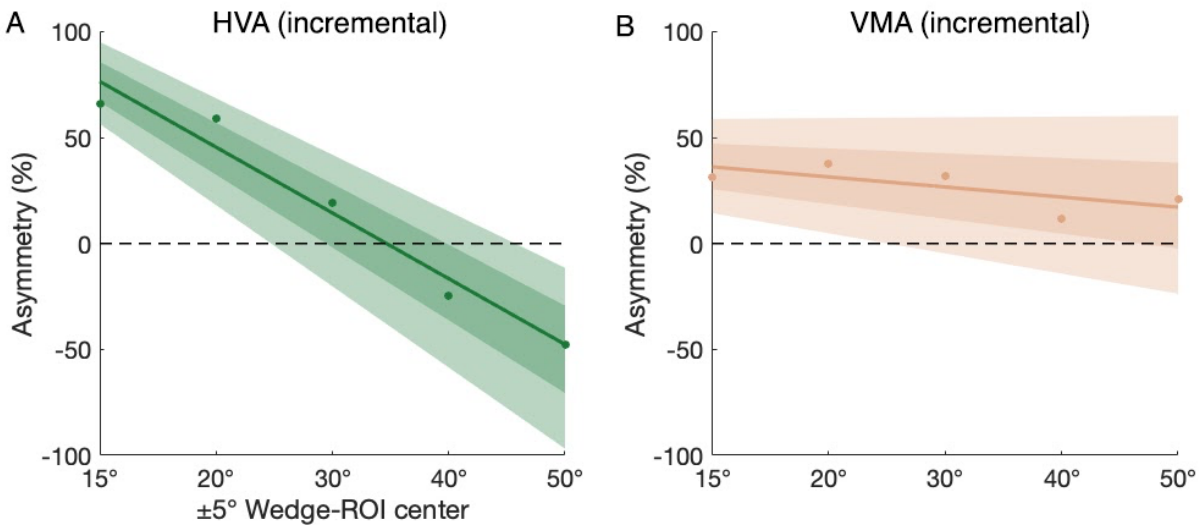

Figure S5. Incremental HVA and VMA asymmetries for a ±5° wedge centered at 5 different locations from the visual field meridians. The HVA and VMA decrease with increasing distance from a cardinal meridian. The incremental HVA becomes inverted because a ±5° wedge centered 50° from the horizontal meridian is closer to the vertical than the horizontal meridian (i.e., beyond 45°). This is the same for a ±5° wedge centered 50° from the vertical meridian; It will be closer to the horizontal than the vertical meridian, so the flip is expected.